

SMAI-JCM

SMAI JOURNAL OF COMPUTATIONAL MATHEMATICS

Tensor-Product Discretization for the Spatially Inhomogeneous and Transient Boltzmann Equation in Two Dimensions

PHILIPP GROHS, RALF HIPTMAIR & SIMON PINTARELLI
Volume 3 (2017), p. 219-248.

http://smai-jcm.cedram.org/item?id=SMAI-JCM_2017__3__219_0

© Société de Mathématiques Appliquées et Industrielles, 2017
Certains droits réservés.

cedram

Article mis en ligne dans le cadre du
Centre de diffusion des revues académiques de mathématiques
<http://www.cedram.org/>





Tensor-Product Discretization for the Spatially Inhomogeneous and Transient Boltzmann Equation in Two Dimensions

PHILIPP GROHS¹
RALF HIPTMAIR²
SIMON PINTARELLI³

¹ University of Vienna, Faculty of Mathematics

E-mail address: philipp.grohs@univie.ac.at

² ETH Zürich, Seminar for Applied Mathematics

E-mail address: ralf.hiptmair@sam.math.ethz.ch

³ ETH Zürich, Seminar for Applied Mathematics

E-mail address: simon.pintarelli@sam.math.ethz.ch.

Abstract. We consider the spatially inhomogeneous and nonlinear Boltzmann equation for the variable hard spheres model. The distribution function is discretized by a tensor-product ansatz by combining Maxwellian modulated Laguerre polynomials in velocity with continuous, linear finite elements in the spatial domain. The advection problem in phase space is discretized through a Galerkin least squares technique and yields an implicit formulation in time. The discrete collision operator can be evaluated with an asymptotic effort of $\mathcal{O}(K^5)$, where K is the number of velocity degrees of freedom in a single direction. Numerical results in 2D are presented for rarefied gases with different Mach and Knudsen numbers.

Math. classification. 76J20, 76H05, 76P05, 82C40, 82D05, 65Y05, 65M60.

1. Introduction

The Boltzmann equation offers a mesoscopic description of rarefied gases and is a typical representative of a class of integro partial differential equations that model interacting particle systems. The binary particle interactions in d -dimensional space are modeled by a collision operator which involves a $2d - 1$ fold integral. Due to its non-linearity and the high dimension, the evaluation of the collision operator is computationally challenging. Stochastic simulation methods are widely used. A well-known example is the direct simulation Monte Carlo (DSMC) method developed by Bird and Nanbu in [3] and [23]. Among deterministic approaches Fourier methods are most popular. In [25] Pareschi et al. introduced a Fourier based method, related approaches have been introduced in [4, 5, 15, 30]. Fourier methods are fairly efficient and accurate for short-time simulations, but they suffer from aliasing errors caused by the periodic truncation of the velocity domain. Another problem of the Fourier spectral method is that it does not capture the correct long-time behaviour, unless the steady state preserving modification [12] is employed.

To overcome these problems a spectral discretization in velocity based on Laguerre polynomials has been developed in [13] for the spatially homogeneous Boltzmann equation extending the work done in [9]. For this method, no truncation of the velocity domain is necessary and the natural conserved quantities can be easily preserved by the numerical scheme. As a consequence, the velocity-spectral method enjoys the correct long-term behaviour, while the aliasing effects incurred by the plain Fourier spectral method will in general lead to unphysical solutions (see Section 6.1). Additionally, this approach has the advantage that no periodic truncation is needed and the collision operator can be represented as a tensor, which enjoys considerable sparsity and whose entries can be precomputed with highly accurate quadrature.

Closely related and conducted parallel to our investigations is the work by Kitzler and Schöberl [14, 22]. These authors also use a spectral polynomial discretization in velocity, but they rely on a Petrov-Galerkin discretization. The velocity distribution function (VDF) is represented by polynomials times a shifted Maxwellian, while the test functions are polynomials. The complexity for the evaluation of the collision operator is reduced from $\mathcal{O}(K^6)$ to $\mathcal{O}(K^5)$ by exploiting its translation invariance. They locally rescale the basis functions in velocity to fit macroscopic velocity and temperature. In physical space Kitzler and Schöberl use a discontinuous Galerkin scheme. On the one hand this offers great flexibility concerning the local choice of velocity spaces. On the other hand the DG method involves evaluating interface fluxes and thus requires projection of the velocity distribution function between adjacent elements. Then stability issues impose constraints on the temperature differences between neighboring elements.

In this work, we extend this idea to the spatially inhomogeneous Boltzmann equation, combining a truncation-free spectral Galerkin approximation in velocity with a least squares stabilized finite element discretization in space. The tensor based local evaluation of the discrete collision operator involves an asymptotic computational effort of $\mathcal{O}(K^5)$, where K is the polynomial degree in one velocity direction, see Section 4. We also explore ways to ensure discrete conservation of mass, momentum, and energy, see Section 4.2. This can be achieved by direct enforcement of the constraints through Lagrangian multipliers. For time-stepping we rely on a splitting scheme, which separately treats collisions and advection. For the former we opt for explicit time-stepping, whereas the latter is tackled by a time-implicit least squares formulation. This has the advantage, that for high Knudsen numbers we are not restricted by a CFL condition. However one must note that for small Knudsen numbers, i.e. small mean free path length, the problem is stiff and the time-step must be chosen sufficiently small. Extensive numerical tests in various settings typical of flow problems for rarefied gases are reported in Section 6.

The outline of the paper is as follows: In Section 2 we introduce the Boltzmann equation and its properties that are used in the sequel. The conservative scheme for the homogeneous Boltzmann equation is discussed in Section 4, followed by the extension to the spatially inhomogeneous case in Section 5. Numerical results for a range of benchmark problems are reported in Section 6.

2. The Boltzmann equation

The time-dependent distribution function $f = f(\mathbf{x}, \mathbf{v}, t)$ is sought on the 2+2-dimensional phase space $\Omega = D \times \mathbb{R}^2$, where $D \subset \mathbb{R}^2$ denotes a bounded spatial domain with piecewise smooth boundary.

We consider the inhomogeneous and time dependent Boltzmann equation

$$\partial_t f + \mathbf{v} \cdot \nabla_{\mathbf{x}} f = \frac{1}{\epsilon} Q(f, f)(\mathbf{v}), \quad (\mathbf{x}, \mathbf{v}) \in \Omega = D \times \mathbb{R}^2, \quad (2.1)$$

with initial distribution

$$f(\mathbf{x}, \mathbf{v}, t = 0) = f_0(\mathbf{x}, \mathbf{v}), \quad (2.2)$$

and the Boltzmann collision operator Q , which in $2D$ is represented by a 3 fold integral:

$$Q(f, h)(\mathbf{v}) = \int_{\mathbb{R}^2} \int_{\mathbb{S}^1} B(\|\mathbf{v} - \mathbf{v}_*\|, \cos \theta) (h'_* f' - h_* f) \, d\sigma \, d\mathbf{v}_*, \quad (2.3)$$

where $f = f(\mathbf{v})$, $f' = f(\mathbf{v}')$, $h_* = h(\mathbf{v}_*)$, $h'_* = h(\mathbf{v}'_*)$ and \mathbb{S}^1 denotes the unit circle. For elastic scattering, the post-collisional velocities \mathbf{v}' , \mathbf{v}'_* are given by, see Fig. 2.1:

$$\mathbf{v}' = \frac{\mathbf{v} + \mathbf{v}_*}{2} + \sigma \frac{\|\mathbf{v} - \mathbf{v}_*\|}{2}, \quad \mathbf{v}'_* = \frac{\mathbf{v} + \mathbf{v}_*}{2} - \sigma \frac{\|\mathbf{v} - \mathbf{v}_*\|}{2} \quad \sigma \in \mathbb{S}^1. \quad (2.4)$$

Given sufficient regularity of the collision kernel B , it is convenient to split Q into gain Q^+ and loss Q^- part

$$Q^+(f, h)(\mathbf{v}) = \int_{\mathbb{R}^2} \int_{\mathbb{S}^1} B(\|\mathbf{v} - \mathbf{v}_*\|, \cos \theta) h'_* f' \, d\sigma \, d\mathbf{v}_* \quad (2.5)$$

$$Q^-(f, h)(\mathbf{v}) = \int_{\mathbb{R}^2} \int_{\mathbb{S}^1} B(\|\mathbf{v} - \mathbf{v}_*\|, \cos \theta) h_* f \, d\sigma \, d\mathbf{v}_*. \quad (2.6)$$

The Knudsen number ϵ represents the ratio of the mean free path to a representative physical length scale. Boundary conditions are prescribed on the inflow boundary $\Gamma^-, \Gamma^\pm := \{(\mathbf{x}, \mathbf{v}) : \mathbf{x} \in \partial D \wedge \mp \mathbf{v} \cdot \mathbf{n} < 0\}$, where \mathbf{n} denotes the outward unit normal vector field. Common types of boundary conditions are inflow, specular reflective, and diffusive reflective boundary conditions [28, Section 1.5]:

$$\textbf{Inflow boundary conditions:} \quad f(t, \mathbf{x}, \mathbf{v}) = f_{in}(t, \mathbf{x}, \mathbf{v}), \quad (\mathbf{x}, \mathbf{v}) \in \Gamma^- \quad (2.7)$$

$$\textbf{Specular reflective b.c.:} \quad f(t, \mathbf{x}, \mathbf{v}) = f(t, \mathbf{x}, \mathbf{v} - 2\mathbf{v} \cdot \mathbf{nn}), \quad (\mathbf{x}, \mathbf{v}) \in \Gamma^- \quad (2.8)$$

$$\textbf{Diffusive reflective b.c.:} \quad f(t, \mathbf{x}, \mathbf{v}) = M_w(\mathbf{x}, \mathbf{v}) \rho_+(f), \quad (\mathbf{x}, \mathbf{v}) \in \Gamma^-, \quad (2.9)$$

where

$$M_w(\mathbf{x}, \mathbf{v}) := \left(\frac{1}{2\pi}\right)^{\frac{1}{2}} T_w^{\frac{3}{2}} e^{-\frac{\|\mathbf{v}\|^2}{2T_w}}, \quad (2.10)$$

is a Maxwellian distribution at the boundary, which may depend on \mathbf{x} implicitly through the wall temperature $T_w(\mathbf{x})$, and

$$\rho_+(f) := \int_{\Gamma^+} \mathbf{n} \cdot \mathbf{w} f(t, \mathbf{x}, \mathbf{w}) \, d\mathbf{w}.$$

M_w is normalized such that $\int_{\Gamma^+} \mathbf{n} \cdot \mathbf{v} M_w(\mathbf{x}, \mathbf{v}) \, d\mathbf{v} = 1$.

Macroscopic quantities of the gas can be computed in terms of moments of the distribution function f .

$$\begin{aligned} \text{Mass density} \quad \rho(t, \mathbf{x}) &= \int_{\mathbb{R}^2} f(t, \mathbf{x}, \mathbf{v}) \, d\mathbf{v} \\ \text{Momentum density} \quad \mathbf{u}(t, \mathbf{x}) &= \frac{1}{\rho} \int_{\mathbb{R}^2} \mathbf{v} f(t, \mathbf{x}, \mathbf{v}) \, d\mathbf{v} \\ \text{Energy density} \quad E(t, \mathbf{x}) &= \frac{1}{\rho} \int_{\mathbb{R}^2} \|\mathbf{v}\|^2 f(t, \mathbf{x}, \mathbf{v}) \, d\mathbf{v} \\ \text{Temperature} \quad T(t, \mathbf{x}) &= \frac{1}{2} (E(t, \mathbf{x}) - \|\mathbf{u}(t, \mathbf{x})\|^2) \end{aligned}$$

We assume that the interaction potential governing collisions is described by a collision kernel B of the form [28]:

$$B(\|\mathbf{v} - \mathbf{v}_*\|, \cos \theta) = C(\cos \theta) \|\mathbf{v} - \mathbf{v}_*\|^\lambda, \quad (2.11)$$

and that $C(\cos \theta)$ satisfies Grad's cutoff assumption [17]: $\int_0^{2\pi} C(\cos \theta) \, d\theta < \infty$.

In the following, we will restrict ourselves to the variable hard spheres model, i.e. we set $C \equiv \frac{1}{2\pi}$ and consider $0 \leq \lambda \leq 1$. The case $\lambda = 0$ is known as Maxwellian molecules. In order to reduce the computational complexity we will make use of the rotational and translational invariance of the collision operator Q . The pullbacks induced by the translation $\tau^*(\mathbf{c})$ and rotation operator $\rho^*(\omega)$ act on a function $f : \mathbb{R}^2 \rightarrow \mathbb{R}$ as follows:

$$\begin{aligned} \tau^*(\mathbf{c})f(\mathbf{v}) &:= f(\mathbf{v} + \mathbf{c}), & \text{for } \mathbf{c} \in \mathbb{R}^2 \quad (\text{in Cartesian coordinates}) \\ \rho^*(\omega)f(\varphi, r) &:= f(\varphi + \omega, r), & \text{for } \omega \in [0, 2\pi[\quad (\text{in polar coordinates}) \end{aligned}$$

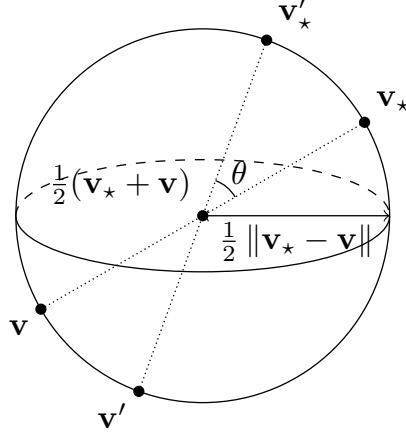


FIGURE 2.1. Pre- and post-collisional velocities $\mathbf{v}, \mathbf{v}_*, \mathbf{v}', \mathbf{v}'_*$ for elastic collisions.

It is easy to see that the collision operator enjoys the following covariance properties:

$$Q(\rho^*(\omega)f, \rho^*(\omega)g)(\varphi, r) = \rho^*(\omega)Q(f, g)(\varphi, r), \quad \forall(\varphi, r) \quad (2.12)$$

$$Q(\tau^*(\mathbf{c})f, \tau^*(\mathbf{c})g)(\mathbf{v}) = \tau^*(\mathbf{c})Q(f, g)(\mathbf{v}), \quad \forall \mathbf{v} \quad (2.13)$$

for any $\omega \in [0, 2\pi[$ and $\mathbf{c} \in \mathbb{R}^2$.

3. Spectral Velocity Space

In the velocity coordinate, we use Maxwellian weighted tensor product polynomials and their representation in the *Polar-Laguerre* basis developed in [14, Section 2.1]. It can be shown, that the basis spans the space of weighted polynomials in \mathbb{R}^2 of total degree $\leq K$, with weight $e^{-r^2/2}$. Throughout we designate by (φ, r) polar coordinates in \mathbb{R}^2 .

Definition 3.1 (Polar-Laguerre basis functions $\Psi_{k,j}^a(\varphi, r)$).

$$\Psi_{k,j}^\xi(\varphi, r) := \begin{cases} \xi(2j\varphi) r^{2j} L_{\frac{k}{2}-j}^{(2j)}(r^2) e^{-r^2/2} & k \in 2\mathbb{N} \\ \xi((2j+1)\varphi) r^{2j+1} L_{\frac{k-1}{2}-j}^{(2j+1)}(r^2) e^{-r^2/2} & k \in 2\mathbb{N} + 1 \end{cases} \quad (3.1)$$

where $\xi = \cos, \sin$ and $L_n^{(\alpha)}$ are the associated Laguerre polynomials [1].

The basis functions $\Psi_{k,j}^\xi$ are orthogonal in the inner product $\langle f, g \rangle := \int_{\mathbb{R}^2} f(\mathbf{v})g(\mathbf{v}) d\mathbf{v}$ [1, Chap. 22].

Definition 3.2 (Polar-Laguerre basis $\mathfrak{B}_{\mathcal{L}}^N$). The set

$$\mathfrak{B}_{\mathcal{L}}^N := \{\mathbb{L}_k^{\cos} : k = 0, \dots, K\} \cup \{\mathbb{L}_k^{\sin} : k = 0, \dots, K\}, \quad (3.2)$$

where

$$\mathbb{L}_k^{\cos} := \{\Psi_{k,j}^{\cos} : j = 0 \dots \lfloor \frac{k}{2} \rfloor\}, \quad \mathbb{L}_k^{\sin} := \{\Psi_{k,j}^{\sin} : j = 1 - (k \bmod 2) \dots \lfloor \frac{k}{2} \rfloor\}. \quad (3.3)$$

According [14, Lemma 5] $\mathfrak{B}_{\mathcal{L}}^N$ is a basis for the space of polynomials in \mathbb{R}^2 of maximal degree K weighted by $e^{-r^2/2}$. For later use we define also the function space $V_{\mathcal{V}}^N := \text{span}\{\mathfrak{B}_{\mathcal{L}}^N\}$. Throughout, $N := K(K+1)/2$ will always denote the number of basis functions used to discretize the velocity domain and has therefore been included in the superscript of the symbols $\mathfrak{B}_{\mathcal{L}}^N$ and $V_{\mathcal{V}}^N$. The structure

of the Polar-Laguerre basis functions allows to exploit the rotation invariance (2.12) in order to obtain a sparse discretization of the collision operator, cf. Section 4.1.

Whenever convenient, we will drop the double index (k, j) of $\Psi_{k,j}$ and denote elements of $\mathfrak{B}_{\mathcal{L}}^N$ by $b_i, i = 0, \dots, N - 1$. Thus we may formally write the expansion of a function $f \in V_{\mathcal{V}}^N$ with Polar-Laguerre coefficients $c_j^P, j = 0, \dots, N - 1$:

$$f^N(\varphi, r) := \sum_{j=0}^{N-1} c_j^P b_j(\varphi, r). \quad (3.4)$$

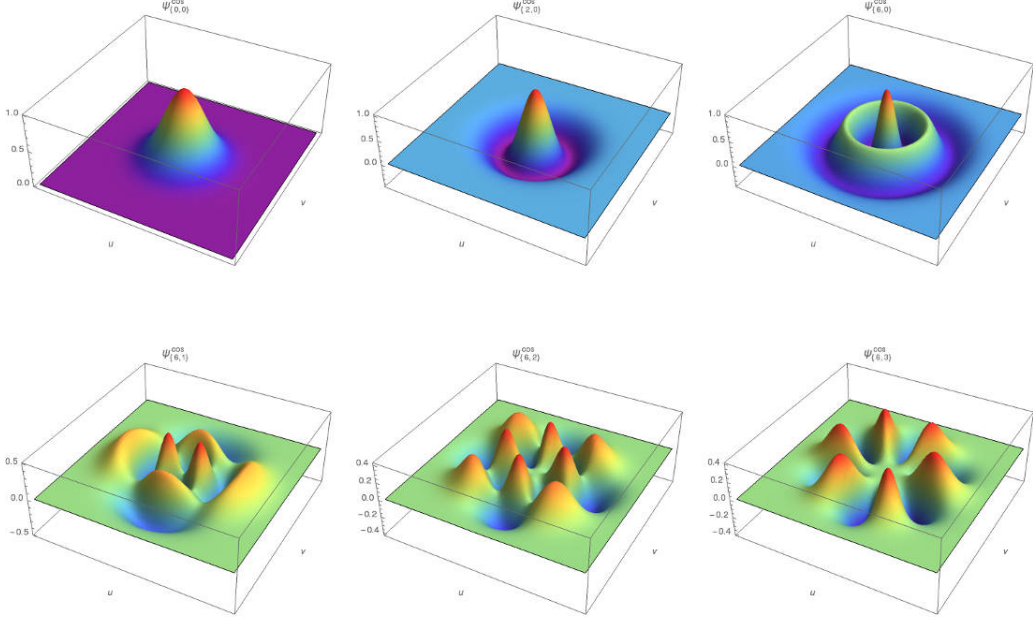


FIGURE 3.1. Polar-Laguerre basis functions $\Psi_{k,j}^{\text{cos}}(\mathbf{v})$, $\mathbf{v} \in [-5, 5]^2$.
First row: $j = 0, k = 0, 2, 6$, **Second row:** $k = 6, j = 1, 2, 3$.

For some operations on the velocity distribution function it is more efficient, from an algorithmic point of view, to switch to other bases: the nodal and the Hermite basis. The transformation between Polar-Laguerre and nodal basis representation can be done in an efficient manner by using the Hermite basis as an intermediate, see Sections 4.4, 6.2.

Definition 3.3 (Hermite basis). The set of functions $\mathbb{R}^2 \rightarrow \mathbb{R}$

$$\mathfrak{B}_{\mathcal{H}}^N := \left\{ (x, y) \mapsto h_s(x) h_{k-s}(y) e^{-\frac{x^2+y^2}{2}} : 0 \leq k \leq K \wedge 0 \leq s \leq k \right\} \quad (3.5)$$

where $h_i(x)$ are suitably normalized Hermite polynomials [1], such that $\int_{\mathbb{R}} h_i(x) h_j(x) e^{-x^2} dx = \delta_{i,j}$, is called Hermite basis, the functions $h_j(x) e^{-\frac{x^2}{2}}$ are Hermite basis functions.

Definition 3.4 (Nodal basis). The set of functions $\mathbb{R}^2 \rightarrow \mathbb{R}$

$$\mathfrak{B}_{\mathcal{N}} := \left\{ (x, y) \mapsto l_i(x) l_j(y) e^{-\frac{x^2+y^2}{2}} : 0 \leq i, j \leq K \right\} \quad (3.6)$$

is called nodal basis. The ℓ_i denote the Lagrange polynomials at the Gauss-Hermite quadrature nodes x_i with weights w_i [1].

$$\ell_i(x) := \frac{1}{\sqrt{w_i}} \prod_{\substack{0 \leq m \leq K \\ m \neq i}} \frac{x - x_m}{x_i - x_m}.$$

The $\ell_i(x)$ are normalized such that $\int_{\mathbb{R}} \ell_i(x) \ell_j(x) e^{-x^2} dx = \delta_{i,j}$.

The nodal basis will be used in Section 6 to project the velocity distribution function to positive values. It also plays a role in the code for the application of boundary conditions (details will be discussed in a separate publication).

Lemma 3.5. [14, Lemma 5] *The set of basis functions $\mathfrak{B}_{\mathcal{L}}^N$ and $\mathfrak{B}_{\mathcal{H}}^N$ (cf. (3.2), Definition 3.3) span the same function space $V_{\mathcal{V}}^N$, that is the space of polynomials of maximal degree K with weight function $e^{-\|v\|^2/2}$, see Definition 3.2. Also observe that $V_{\mathcal{V}}^N \subset \text{span } \mathfrak{B}_{\mathcal{N}}$ and $\dim \text{span } \mathfrak{B}_{\mathcal{N}} = (K + 1)^2$.*

Notation. In the following, we will tag coefficient vectors \mathbf{c} with a superscript P, H, N to indicate that they belong to the Polar-Laguerre, Hermite or the nodal basis.

4. Treatment of the Collision Operator

In this section we will discuss the discretization of the collision operator.

4.1. Discretization in velocity coordinate

The following derivation is identical to the one presented in [13], except that we use a real valued basis in φ . Consider the homogeneous Boltzmann equation

$$\partial_t f = Q(f, f). \quad (4.1)$$

Multiplication of (4.1) with a test function $g \in V_{\mathcal{V}}^N$ and integration over \mathbb{R}^2 gives

$$\partial_t \int_{\mathbb{R}^2} f(t, \mathbf{v}) g(\mathbf{v}) d\mathbf{v} = \int_{\mathbb{R}^2} Q(f, f) g(\mathbf{v}) d\mathbf{v}. \quad (4.2)$$

Expanding f in a basis $\{b_l\}_{l=1}^N$ of $V_{\mathcal{V}}^N$ and choosing $g = b_i \in V_{\mathcal{V}}^N$ gives rise to a 3-dimensional tensor Q_N . One may think of it as an array of $N \times N$ matrices $\mathbf{S}_i, i = 0, \dots, N - 1$, where slice \mathbf{S}_i is obtained by testing with $b_i \in V_{\mathcal{V}}^N$:

$$(\mathbf{S}_i)_{i_1, i_2} := \langle Q(b_{i_1}, b_{i_2}), b_i \rangle_{L^2(\mathbb{R}^2)}, \quad b_i, b_{i_1}, b_{i_2} \in \mathfrak{B}_{\mathcal{L}}^N \quad (4.3)$$

We split $Q(f, f) = Q^+(f, f) - Q^-(f, f)$, as in (2.5) and (2.6), and accordingly $\mathbf{S} = \mathbf{S}^+ - \mathbf{S}^-$.

$$\begin{aligned} (\mathbf{S}_i^-)_{i_1, i_2} &= \langle Q^-(b_{i_1}, b_{i_2}), b_i \rangle = \int_{\mathbb{R}^2} \int_{\mathbb{R}^2} \int_{\mathbb{S}^1} B(\|\mathbf{v} - \mathbf{v}_\star\|, \cos \theta) b_{i_1}(\mathbf{v}) b_{i_2}(\mathbf{v}_\star) b_i(\mathbf{v}) d\sigma d\mathbf{v}_\star d\mathbf{v} \\ &= \int_{\mathbb{R}^2} b_{i_1}(\mathbf{v}) b_i(\mathbf{v}) \int_{\mathbb{R}^2} b_{i_2}(\mathbf{v}_\star) \mathcal{I}^-(\mathbf{v}, \mathbf{v}_\star) d\mathbf{v}_\star d\mathbf{v}, \end{aligned} \quad (4.4)$$

where the *inner integral* \mathcal{I}^- is given by

$$\mathcal{I}^- = \int_{\mathbb{S}^1} B(\|\mathbf{v} - \mathbf{v}_\star\|, \cos \theta) d\sigma = \|\mathbf{v} - \mathbf{v}_\star\|^\lambda \int_{\mathbb{S}^1} C(\cos \theta) d\sigma, \quad (4.5)$$

and as stated in the beginning, for Maxwellian molecules $C \equiv \frac{1}{2\pi}$.

$$\begin{aligned}
 [\mathbf{S}_i^+]_{(i_1, i_2)} &= \langle Q^+(b_{i_1}, b_{i_2}), b_i \rangle_{L^2(\mathbb{R}^2)} = \int_{\mathbb{R}^2} \int_{\mathbb{R}^2} \int_{\mathbb{S}^1} B(\|\mathbf{v} - \mathbf{v}_\star\|, \cos \theta) b_{i_1}(\mathbf{v}') b_{i_2}(\mathbf{v}'_\star) b_i(\mathbf{v}) \, d\sigma \, d\mathbf{v}_\star \, d\mathbf{v} \\
 &= \int_{\mathbb{R}^2} \int_{\mathbb{R}^2} b_{i_1}(\mathbf{v}) b_{i_2}(\mathbf{v}_\star) \mathcal{I}^{(+)}(\mathbf{v}, \mathbf{v}_\star; b_i) \, d\mathbf{v}_\star \, d\mathbf{v},
 \end{aligned} \tag{4.6}$$

with

$$\mathcal{I}^{(+)}(\mathbf{v}', \mathbf{v}'_\star; b_i) = \int_{\mathbb{S}^1} B(\|\mathbf{v}' - \mathbf{v}'_\star\|, \cos \theta) b_i(\mathbf{v}') \, d\sigma, \tag{4.7}$$

see (2.4) and Fig. 2.1 for the definition of θ and \mathbf{v}' , \mathbf{v}'_\star . Note that, in the second line of (4.6), we have made the change of variables $\mathbf{v}, \mathbf{v}_\star \leftrightarrow \mathbf{v}', \mathbf{v}'_\star$. Next, we substitute $\mathbf{w}' = \mathbf{R}_\alpha \mathbf{v}'$ for $\alpha = -\arg(\mathbf{v} + \mathbf{v}_\star)$. \mathbf{R}_α denotes the rotation by α around the origin in counter clockwise direction. Also note, that the test functions b_i from Definition 3.1 are of the form $\xi(l\varphi) \phi_r(r)$, where ξ is either sin or cos.

$$\begin{aligned}
 \mathcal{I}^{(+)}(\mathbf{v}', \mathbf{v}'_\star; b_i) &= \|\mathbf{v}' - \mathbf{v}'_\star\|^\lambda C \int_{\mathbb{S}^1} b_i(\arg(\mathbf{w}') + \alpha, \|\mathbf{w}'\|) \, d\sigma \\
 &= \|\mathbf{v}' - \mathbf{v}'_\star\|^\lambda C \int_{\mathbb{S}^1} \xi(l(\arg(\mathbf{w}') + \alpha)) \phi_r(\|\mathbf{w}'\|) \, d\sigma
 \end{aligned} \tag{4.8}$$

We simplify (4.8) for $\xi = \sin$

$$\begin{aligned}
 \mathcal{I}^{(+)}(\mathbf{v}', \mathbf{v}'_\star; b_i) &= \|\mathbf{v}' - \mathbf{v}'_\star\|^\lambda C \int_{\mathbb{S}^1} \left[\sin(l \arg(\mathbf{w}')) \cos(l\alpha) + \cos(l \arg(\mathbf{w}')) \sin(l\alpha) \right] \phi_r(\|\mathbf{w}'\|) \, d\sigma \\
 &= \sin(l\alpha) \|\mathbf{v}' - \mathbf{v}'_\star\|^\lambda C \int_{\mathbb{S}^1} \cos(l \arg(\mathbf{w}')) \phi_r(\|\mathbf{w}'\|) \, d\sigma,
 \end{aligned} \tag{4.9}$$

and for $\xi = \cos$

$$\begin{aligned}
 \mathcal{I}^{(+)}(\mathbf{v}', \mathbf{v}'_\star; b_i) &= \|\mathbf{v}' - \mathbf{v}'_\star\|^\lambda C \int_{\mathbb{S}^1} \left[\cos(l \arg(\mathbf{w}')) \cos(l\alpha) - \sin(l \arg(\mathbf{w}')) \sin(l\alpha) \right] \phi_r(\|\mathbf{w}'\|) \, d\sigma \\
 &= \cos(l\alpha) \|\mathbf{v}' - \mathbf{v}'_\star\|^\lambda C \int_{\mathbb{S}^1} \cos(l \arg(\mathbf{w}')) \phi_r(\|\mathbf{w}'\|) \, d\sigma.
 \end{aligned} \tag{4.10}$$

Thus we have found that, up to a factor, the integral $\mathcal{I}^{(+)}(\mathbf{v}', \mathbf{v}'_\star; b_i)$, which is cheap to compute, depends only on $d := \|\mathbf{v}' - \mathbf{v}'_\star\|$ and on $c := \|\mathbf{v}' + \mathbf{v}'_\star\|$. The 1-dimensional integrals in (4.9) and (4.10) are evaluated numerically using the midpoint rule, details are given in Section 6. The extension to collision kernels of the form (2.11) that depend on the angle θ and satisfy Grad's cut-off assumption is straightforward, but comes with the additional cost that the results for $\mathcal{I}^{(\pm)}$ are no longer functions of only d and c anymore, thus cannot be cached and have to be re-evaluated for all pairs of quadrature points $(\mathbf{v}', \mathbf{v}'_\star)$. The discretized collision operator Q_N has the following expansion into basis functions (the conservative form will be discussed in Section 4.2):

$$Q_N(f, g)(\mathbf{v}) = \sum_{i=1}^N \left[\mathbf{M}^{-1} [\mathbf{c}^T \mathbf{S}_j \mathbf{d}]_{j=1}^N \right]_i b_i(\mathbf{v}), \tag{4.11}$$

where $[\mathbf{M}]_{j,j'} = \langle b_j, b_{j'} \rangle$, $f, g \in V_{\mathcal{V}}^N$ with coefficient vectors \mathbf{c}, \mathbf{d} with respect to the basis $\{b_l\}_{l=1}^N$.

4.2. Conservative discretization

An important property of (4.1) is that mass, momentum and energy are conserved. In particular it holds that

$$\partial_t \begin{pmatrix} \rho(f) \\ \rho \mathbf{u}(f) \\ \rho E(f) \end{pmatrix} = \int_{\mathbb{R}^2} Q(f, f) \begin{pmatrix} 1 \\ \mathbf{v} \\ \|\mathbf{v}\|^2 \end{pmatrix} d\mathbf{v} \equiv 0, \quad (4.12)$$

by fundamental properties of the Boltzmann collision operator [6, sec. 5].

Galerkin discretization with Lagrange multipliers. In order to enforce condition (4.12) we use a Galerkin discretization and solve a L^2 least squares problem such that mass, momentum and energy are conserved. This has been proposed in [15] for the Fourier-spectral method. In the context of a time-stepping method for the homogeneous Boltzmann equation, let \mathbf{c}^k be the coefficient vector in the Polar-Laguerre basis at time t_k .

- (1) Compute coefficients at the next time-step by a single step of an explicit time-stepping scheme, here explicit Euler:

$$\tilde{\mathbf{c}}^{k+1} = \mathbf{c}^k + \frac{1}{\epsilon} \Delta t_k Q_N(\mathbf{c}^k, \mathbf{c}^k)$$

- (2) Solve the saddle point problem:

$$\mathbf{c}^{k+1} = \arg \min_{\mathbf{c}_*^{k+1} \in \mathbb{R}^N} \left\| \mathbf{c}_*^{k+1} - \tilde{\mathbf{c}}^{k+1} \right\|^2 + \underbrace{\lambda^T \mathbf{H}^T (\mathbf{c}_*^{k+1} - \mathbf{c}^k)}_{\text{conservation of mass, momentum and energy}}, \quad (4.13)$$

where $\mathbf{H}^T \in \mathbb{R}^{2+2 \times N}$, $\mathbf{H}^T \mathbf{c} = (\rho, \rho \mathbf{u}, \rho E)^T$, with Lagrange multiplier $\lambda \in \mathbb{R}^{2+2}$. The entries of \mathbf{H}^T are given by:

$$\left. \begin{aligned} [\mathbf{H}^T]_{1,i} &= \int_{\mathbb{R}^2} b_i(\mathbf{v}) d\mathbf{v} \\ [\mathbf{H}^T]_{2,i} &= \int_{\mathbb{R}^2} \mathbf{v}_x b_i(\mathbf{v}) d\mathbf{v} \\ [\mathbf{H}^T]_{3,i} &= \int_{\mathbb{R}^2} \mathbf{v}_y b_i(\mathbf{v}) d\mathbf{v} \\ [\mathbf{H}^T]_{4,i} &= \int_{\mathbb{R}^2} \|\mathbf{v}\|^2 b_i(\mathbf{v}) d\mathbf{v}. \end{aligned} \right\} \text{for } b_i \in \mathfrak{B}_{\mathcal{L}}^N, i = 1, \dots, N \quad (4.14)$$

The solution of (4.13) is

$$\mathbf{c}^{k+1} = \tilde{\mathbf{c}}^{k+1} - \frac{1}{2} \mathbf{H} \lambda, \quad (4.15)$$

with

$$\lambda = 2(\mathbf{H}^T \mathbf{H})^{-1} \mathbf{H}^T (\tilde{\mathbf{c}}^{k+1} - \mathbf{c}^k). \quad (4.16)$$

Also note that $\mathbf{H}^T \mathbf{H}$ is positive definite. For the space inhomogeneous case we use a Lie-Trotter splitting to separate the advection and collision part (cf. Section 5 for details). The Lie-Trotter splitting is consistent for evolution problems [20]. Therefore, the procedure described above to conserve moments can be applied independently and in the same way for each degree of freedom in the spatial domain.

4.3. Computational aspects

We repeat Definition 3.1 of the Polar-Laguerre basis functions $\Psi_{k,j}$, and, for the sake of simplicity in the current discussion, replace the real valued Fourier modes by their complex counterparts:

$$\Psi_{k,j}(\varphi, r) := \begin{cases} e^{i 2j\varphi} r^{2j} L_{\frac{k}{2}-j}^{(2j)}(r^2) e^{-r^2/2} & k \in 2\mathbb{N} \\ e^{i(2j+1)\varphi} r^{2j+1} L_{\frac{k-1}{2}-j}^{(2j+1)}(r^2) e^{-r^2/2} & k \in 2\mathbb{N} + 1 \end{cases} \quad (4.17)$$

First, we observe that the $\Psi_{k,j}$'s are of the form $f_\varphi(l\varphi) f_r(r)$ with angular frequency $l \in \mathbb{Z}$.

Corollary 4.1. *Let f and g be represented in polar coordinates as*

$$f(r, \varphi) = f_r(r) e^{i k \varphi}, \quad g(r, \varphi) = g_r(r) e^{i l \varphi}$$

for some functions f_r, g_r and $l, k \in \mathbb{Z}$. Then,

$$Q(f, g)(r, \varphi) = C(r) e^{-i(k+l)\varphi} \quad (4.18)$$

Proof. [13] We get $\rho^*(\omega) f = e^{i k \omega} f$, and correspondingly for g . Using (2.12) and the bilinearity of Q we obtain

$$\rho^*(\omega) Q(f, g)(r, \varphi) = e^{i(k+l)\omega} Q(f, g)(r, \varphi). \quad (4.19)$$

Choose $\omega = -\varphi$ and rearrange to find

$$Q(f, g)(r, \varphi) = e^{-i(k+l)\varphi} \rho^*(\varphi) Q(f, g)(r, \varphi).$$

The result follows since $\rho^*(\varphi) Q(f, g)(r, \varphi) = Q(f, g)(r, 0)$ is independent of φ . \blacksquare

As a direct consequence of Corollary 4.1, in the complex Fourier basis, the collision tensor contains nonzero entries for $l + k = j$ only, where l, k and j are the angular frequencies of the trial function and the test function respectively. In the real valued Fourier basis, we have nonzero entries for $k + l = j$ or $|k - l| = j$ only, the derivation can be found in [18, Appendix].

Corollary 4.2. *The consequence of Corollary 4.1 is that each $\mathbf{S}_i \in \mathbb{R}^{N \times N}$ from (4.11) only has $\mathcal{O}(K^3)$ nonzero entries, and therefore the tensor representation of Q_N has $\mathcal{O}(K^5)$ nonzero entries.*

Remark 4.3. Using similar ideas for spherical harmonics as in Corollary 4.1, it can be shown that the cost of the application of Q^N in 3 dimensions can be reduced from $\mathcal{O}(K^9)$ to $\mathcal{O}(K^8)$, see [29] for details. Also the closely related method pursued in [14] would cost $\mathcal{O}(K^8)$.

Quadrature is carried out in polar coordinates. We use Gauss quadrature nodes and weights in the radial direction r on the interval $[0, \infty]$ with weight $r e^{-r^2/2}$, which are computed via the Golub-Welsch algorithm [16]. Recursion formulas for the coefficients contained in the Jacobi matrix can be found in [27]. Due to numerical instabilities, both the recursion formulas and the eigenvalue problem have to be computed with extended precision. We compute the quadrature nodes and weights with 128 digit accuracy, which is sufficient for degrees up to order ≈ 100 , and store them in tables.

4.4. Exploiting the translational invariance of Q

We have used the rotational invariance of the collision operator for efficient computation and storage of its discrete analogue. According to (2.13), Q is also invariant to translation. A Maxwellian at temperature $T = 1$ with momentum $\mathbf{u} = 0$ is represented in the polar basis by a single non-zero coefficient. In order to represent the same Maxwellian with momentum $\mathbf{u} \neq 0$ with same accuracy, the required polynomial degree K grows with $\|\mathbf{u}\|$, cf. Section 4.4.1. If one wants to apply the collision operator to a given function, it would be beneficial to perform first a change of variables such that it has zero momentum, apply the collision operator and then shift it back to the original position. This

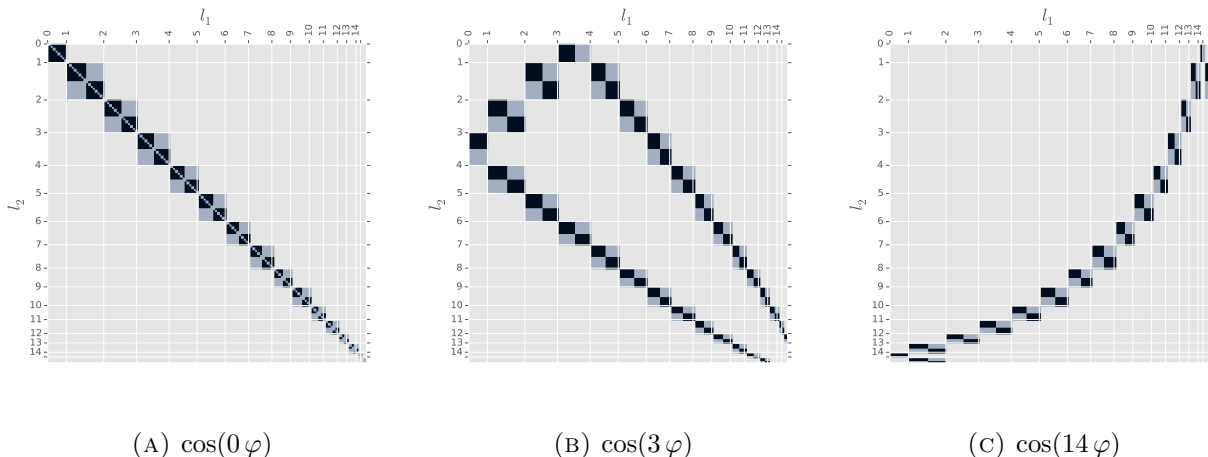


FIGURE 4.1. Nonzero entries for a few slices S_i defined in (4.3) of the collision tensor for $K = 16$. The plots are labeled by the angular part of the test function b_i , since the location of the nonzero entries depend on it solely. The basis functions are lexicographically sorted by the tuple $(l, \cos / \sin, k)$, where l is the angular frequency of \sin / \cos and k denotes the polynomial degree in radial direction.

has the advantage that a given function with zero momentum will have faster decaying coefficients compared to its nonzero momentum counterpart and thus one might truncate at a lower K without loss of accuracy. The straightforward way to translate a given function in its polar representation to zero momentum is to compute the expansion of $f(\mathbf{v} + \mathbf{u})$ in the Polar-Laguerre basis, where \mathbf{u} denotes the momentum. This entails the evaluation of f , which costs $\mathcal{O}(K^2)$, at $\mathcal{O}(K^2)$ quadrature points, resulting in a total cost of $\mathcal{O}(K^4)$. In the following, we will show that this can be done with complexity $\mathcal{O}(K^3)$ if we temporarily switch to the Hermite basis, cf. Definition 3.3. As a consequence of [14, Lemma 5], any function in the Polar-Laguerre basis of degree K has an exact representation through Hermite polynomials of total degree K . Let us formally define the coefficient transformations matrices $\mathbf{T}_{\text{P} \rightarrow \text{H}}$, $\mathbf{T}_{\text{H} \rightarrow \text{P}}$ used to transform Polar-Laguerre to Hermite coefficients and vice versa:

$$\mathbf{c}^{\text{H}} = \mathbf{T}_{\text{P} \rightarrow \text{H}} \mathbf{c}^{\text{P}}, \quad \mathbf{c}^{\text{P}} = \mathbf{T}_{\text{H} \rightarrow \text{P}} \mathbf{c}^{\text{H}},$$

where $\mathbf{T}_{\text{P} \rightarrow \text{H}}, \mathbf{T}_{\text{H} \rightarrow \text{P}} \in \mathbb{R}^{N \times N}$. Because of their block-diagonal structure with dense blocks of size $k+1$, $k=0, \dots, K-1$, the cost to transform the coefficients from the Polar-Laguerre to the Hermite basis is $\mathcal{O}(K^3)$. The derivation of the Polar-Laguerre to Hermite transformation matrices can be found in [22, Section 3.2].

Let c_k denote the coefficients of a 1-dimensional Hermite expansion g with maximal polynomial degree K and momentum \bar{x} . We are looking for the Hermite expansion of $\bar{g}(x) = g(x + \bar{x})$.

$$\bar{g}(x) = g(x + \bar{x}) = \sum_{k=0}^{K-1} c_k h_k(x + \bar{x}) e^{-\frac{(x+\bar{x})^2}{2}} \approx \sum_{k=0}^{K-1} \bar{c}_k h_k(x) e^{-\frac{x^2}{2}} \quad (4.20)$$

Note that $\bar{g}(x)$ has zero momentum. The coefficients \bar{c}_i are computed by forming L_2 -inner products.

$$\begin{aligned} \bar{c}_i &= \int_{\mathbb{R}} \sum_{k=0}^{K-1} c_k h_k(x + \bar{x}) e^{-\frac{(x+\bar{x})^2}{2}} h_i(x) e^{-\frac{x^2}{2}} dx \\ &= \sum_{k=0}^{K-1} c_k \int_{\mathbb{R}} h_k(x + \bar{x}) h_i(x) e^{-\frac{(x+\bar{x})^2}{2}} e^{-\frac{x^2}{2}} dx =: \sum_{k=0}^{K-1} [\mathbf{S}^{\bar{x}}]_{i,k} c_k, \end{aligned} \quad (4.21)$$

The above can be written as a matrix-vector-product $\bar{\mathbf{c}} = \mathbf{S}^{\bar{x}} \mathbf{c}$, where $\mathbf{S}^{\bar{x}} \in \mathbb{R}^{K,K}$. To further simplify the expression for the matrix entries $[\mathbf{S}^{\bar{x}}]_{i,j}$, we substitute $x = x - \frac{\bar{x}}{2}$

$$[\mathbf{S}^{\bar{x}}]_{i,j} = \int_{\mathbb{R}} h_j(x + \frac{\bar{x}}{2}) h_i(x - \frac{\bar{x}}{2}) e^{-x^2} e^{-\frac{\bar{x}^2}{4}} dx \quad (4.22)$$

and use the identity

$$h_n(x + \bar{x}) = \sum_{k=0}^n \binom{n}{k} (2\bar{x})^{n-k} h_k(x), \quad (4.23)$$

to expand $h_k(x + \frac{\bar{x}}{2})$, $h_i(x - \frac{\bar{x}}{2})$, and find

$$\begin{aligned} [\mathbf{S}^{\bar{x}}]_{i,j} &= \frac{1}{\sqrt{i!j!2^{(i+j)/2}}} \sum_{s=0}^i \sum_{t=0}^j \binom{i}{s} \binom{j}{t} (-\bar{x})^{i-s} (\bar{x})^{j-t} e^{-\frac{\bar{x}^2}{4}} \delta_{t,s} 2^t t! \\ &= \frac{1}{\sqrt{i!j!2^{(i+j)/2}}} e^{-\frac{\bar{x}^2}{4}} \sum_{t=0}^{\min(i,j)} \binom{i}{t} \binom{j}{t} (-\bar{x})^{i-t} (\bar{x})^{j-t} 2^t t!, \end{aligned} \quad (4.24)$$

where we have used the orthogonality of the Hermite polynomials.

To carry out the shifting in $2D$, we rearrange the Hermite coefficient vectors \mathbf{c} , $\bar{\mathbf{c}}$ into lower triangular matrices \mathbf{C} , $\bar{\mathbf{C}} \in \mathbb{R}^{K,K}$:

$$f(x, y) = \sum_{i=1}^K \sum_{j=1}^K [\mathbf{C}]_{i,j} h_i(x) e^{-\frac{x^2}{2}} h_j(y) e^{-\frac{y^2}{2}}, \quad (4.25)$$

The matrix $\mathbf{S}^{\bar{x}}$ applied along the columns of \mathbf{C} performs the shift in x -direction, subsequent row-wise application of $\mathbf{S}^{\bar{y}}$ shifts in y -direction:

$$\bar{\mathbf{C}}^T = \mathbf{S}^{\bar{y}} (\mathbf{S}^{\bar{x}} \mathbf{C})^T \Leftrightarrow \bar{\mathbf{C}} = \mathbf{S}^{\bar{x}} \mathbf{C} \mathbf{S}^{\bar{y},T}. \quad (4.26)$$

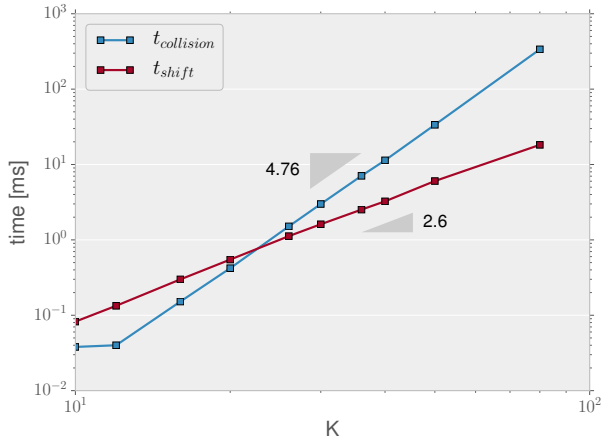
We use orthonormal Hermite polynomials in the implementation to avoid numerical overflow. The procedure described above is summarized in Algorithm 1, whose total cost without evaluating the collision operator is $\mathcal{O}(K^3)$. The coefficients \mathbf{c}^P are sorted by (k, l) , e.g. by increasing polynomial and angular degree, applying the truncated collision operator then means taking only the first $n < N$ rows and columns of each S_i , $i = 0, \dots, N$ in (4.11). The index n is determined such that $|\mathbf{c}_i^P| < \text{tol} \quad \forall i > n$.

Algorithm 1

Collision operator in re-centered basis via Hermite representation. (Superscripts P, H denote coefficients in Polar-Laguerre / Hermite basis.)

- 1: **procedure** APPLY Q_N IN RE-CENTERED BASIS(\mathbf{c}^P)
 - 2: $\mathbf{c}^H \leftarrow \mathbf{T}_{P \rightarrow H} \mathbf{c}^P$ ▷ Transform to Hermite basis
 - 3: $\bar{\mathbf{c}}^H \leftarrow \mathbf{S}^{\bar{x}} \mathbf{c}^H$ ▷ Transform to zero momentum
 - 4: $\bar{\mathbf{c}}^P \leftarrow \mathbf{T}_{H \rightarrow P} \bar{\mathbf{c}}^H$ ▷ Go back to Polar-Laguerre basis
 - 5: $\bar{\mathbf{c}}^P \leftarrow$ update with Q_N in truncated basis
 - 6: $\bar{\mathbf{c}}^H \leftarrow \mathbf{T}_{P \rightarrow H} \bar{\mathbf{c}}^P$ ▷ Transform to Hermite basis
 - 7: $\mathbf{c}^H \leftarrow \mathbf{S}^{-\bar{x}} \bar{\mathbf{c}}^H$ ▷ Shift back
 - 8: $\mathbf{c}^P \leftarrow \mathbf{T}_{H \rightarrow P} \mathbf{c}^H$ ▷ Transform to Polar-Laguerre basis
 - 9: **end procedure**
-

Fig. 4.2 displays timings for the shifting procedure (t_{shift}) and the application of the collision operator ($t_{\text{collision}}$) for varying polynomial degree K . The slopes in the loglog-plot match the predicted



K	$t_{\text{shift}}[ms]$	$t_{\text{collision}}[ms]$
10	0.08	0.04
12	0.13	0.04
16	0.3	0.15
20	0.55	0.42
26	1.12	1.51
30	1.61	2.99
36	2.52	7.08
40	3.25	11.4
50	6.04	33.6
80	18.2	337

FIGURE 4.2. CPU-time: Intel Core i7 4790K (4GHz, single threaded), Linux 4.2.3, GCC 5.2.0, relevant compiler flags: `-O3 -mssse2 -mavx2`. t_{shift} is the time for the execution of Algorithm 1 except the application of the collision operator.

computational complexity of $\mathcal{O}(K^5)$ and $\mathcal{O}(K^3)$ for the collision operator, resp. the shifting procedure. For $K < 26$ shifting cannot pay off, because we observe that it is more time consuming than the application of the collision operator. How much can be gained in terms of wall-clock time by the shifting to zero momentum depends on the number of coefficients that can be neglected for the zero-centered velocity distribution.

4.4.1. Example: Decay of coefficients

The following example is to demonstrate that the Polar-Laguerre coefficients decay fastest if the approximand is centered such that it has zero momentum.

$$f(\mathbf{v}) = \exp(-\mathbf{v}^T \mathbf{W} \mathbf{v}) + \exp(-\frac{\|\mathbf{v}\|^2}{2}), \tag{4.27}$$

where

$$\mathbf{W} = \frac{1}{8} \begin{bmatrix} 7 & \sqrt{3} \\ \sqrt{3} & 5 \end{bmatrix}, \quad \mathbf{v}_c = [\frac{1}{5}, 0]. \tag{4.28}$$

The decay of the absolute values of the Polar-Laguerre coefficients $|\mathbf{c}|$ with respect to angular index $l := 2j + k \pmod 2$ and radial index k is shown in Fig. 4.3.

5. Discretization in Physical Space

In this section we present the spatial discretization in $D \subset \mathbb{R}^2$. It is well known that the advection part in (2.1) requires stabilization. We use a least squares formulation[24, Ch. 10.3.1], which has the advantage that, after partial integration, the term $\langle \mathbf{v} \cdot \mathbf{n} \Phi, f \rangle_\Gamma$ appears in the variational formulation, which comes handy to include inflow-type boundary conditions. The advection part of (2.1) reads

$$\partial_t f + \mathbf{v} \cdot \nabla_{\mathbf{x}} f = 0. \tag{5.1}$$

Tensor-Product Discretization for the Boltzmann Equation

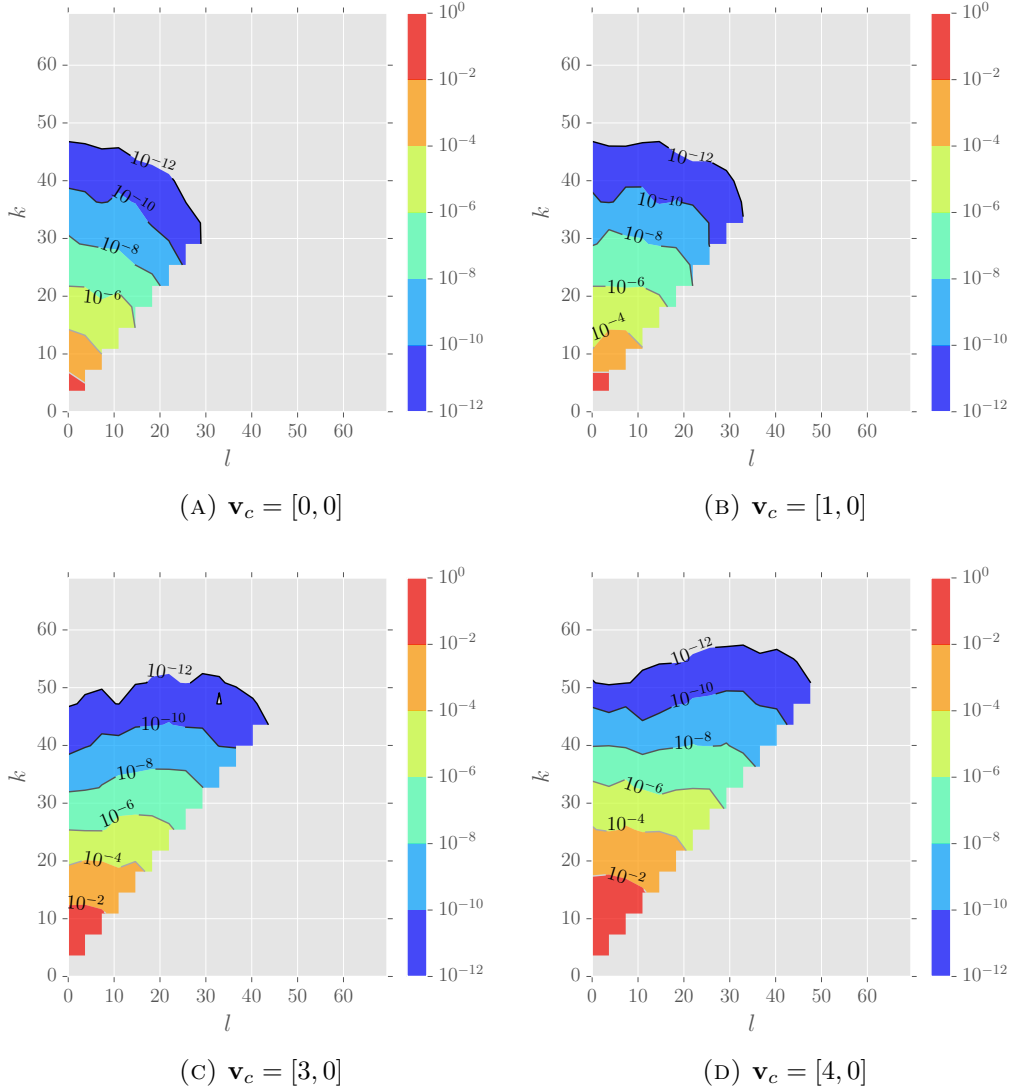


FIGURE 4.3. Decay of Polar-Laguerre coefficients $c_{l,k}$ for $f(\mathbf{v} - \mathbf{v}_c)$, defined in (4.27), with respect to angular index l and radial index k .

We replace $\partial_t f$ in (5.1) by a backwards difference quotient $(\Delta t_k)^{-1}(f^{(n)} - f^{(n-1)})$ and write down the least squares functional $J(f^{(n)}; f^{(n-1)})$ for the pure transport problem [24, Ch. 10.3.1]:

$$J(f^{(n)}; f^{(n-1)}) := \left\| \frac{1}{\Delta t} (f^{(n)} - f^{(n-1)}) + \mathbf{v} \cdot \nabla_{\mathbf{x}} f^{(n)} \right\|_{L^2(\Omega)}^2 \quad (5.2)$$

The bilinear form a and right hand side linear form b of the associated variational problem are given by

$$a(\Phi, f^{(n)}) = \frac{1}{\Delta t^2} \langle \Phi, f^{(n)} \rangle_{\Omega} + \frac{1}{\Delta t} \langle \mathbf{v} \cdot \mathbf{n} \Phi, f^{(n)} \rangle_{\Gamma} + \langle \mathbf{v} \cdot \nabla_{\mathbf{x}} \Phi, \mathbf{v} \cdot \nabla_{\mathbf{x}} f^{(n)} \rangle_{\Omega}, \quad (5.3)$$

where we have used partial integration in \mathbf{x} to obtain the boundary term, and

$$b(\Phi, f^{(n-1)}) := \frac{1}{\Delta t^2} \langle \Phi, f^{(n-1)} \rangle_{\Omega} + \frac{1}{\Delta t} \langle \mathbf{v} \cdot \nabla_{\mathbf{x}} \Phi, f^{(n-1)} \rangle_{\Omega}, \quad (5.4)$$

where \mathbf{n} is the unit outward normal vector on ∂D and $\Gamma := \partial D \times \mathbb{R}^2$. In the following we use $\langle \cdot, \cdot \rangle$ to denote the L_2 -inner product. V_D^L is the space of linear, piecewise continuous finite elements on quadrilateral triangulations of $D \subset \mathbb{R}^2$. The VDF on phase space $\Omega = D \times \mathbb{R}^2$ is approximated in the tensor product space $V^{L,N} = V_D^L \otimes V_V^N$. The test functions Φ are also taken from $V^{L,N}$. We arrive at the following linear system:

$$a(\Phi, f^{(n)}) = b(\Phi, f^{(n-1)}) \quad \forall \Phi \in V^{L,N}. \quad (5.5)$$

The superscript L will denote the number of degrees of freedom in the spatial domain. The system matrix associated to the bilinear form a is sparse and of size $L \times N$. The inclusion of boundary conditions is done in a weak sense, details will be discussed in the next section. When inflow boundary conditions are present, the corresponding parts of $\langle \mathbf{v} \cdot \mathbf{n} \Phi, f \rangle_{\Gamma}$ enter the right hand side.

For integration in time we separate (2.1) into advection and collision part and use a first order split time-stepping:

(1) **Advection** $\partial_t f + \mathbf{v} \cdot \nabla_{\mathbf{x}} f = 0$ (implicit Euler)

$$\begin{aligned} \frac{1}{\Delta t_k^2} \langle \Phi, f^{(n+1/2)} \rangle_{\Omega} + \frac{1}{\Delta t_k} \langle \mathbf{v} \cdot \mathbf{n} \Phi, f^{(n+1/2)} \rangle_{\Gamma} + \langle \mathbf{v} \cdot \nabla_{\mathbf{x}} \Phi, \mathbf{v} \cdot \nabla_{\mathbf{x}} f^{(n+1/2)} \rangle_{\Omega} \\ = \frac{1}{\Delta t_k^2} \langle \Phi, f^{(n)} \rangle_{\Omega} + \frac{1}{\Delta t_k} \langle \mathbf{v} \cdot \nabla_{\mathbf{x}} \Phi, f^{(n)} \rangle_{\Omega} \end{aligned} \quad (5.6)$$

(2) **Collision operator** (explicit Euler)

$$f^{(n+1)} = f^{(n+1/2)} + \frac{\Delta t_k}{\epsilon} Q(f^{(n+1/2)}, f^{(n+1/2)}) \quad (5.7)$$

Remark 5.1. The discrete formulation does not conserve mass for diffusive reflective boundary conditions, because in general, the velocity distribution function will have jumps across the line $\mathbf{v} \cdot \mathbf{n} \equiv 0$. Discontinuous functions cannot be represented exactly in the Polar-Laguerre basis and therefore mass only is conserved asymptotically. In the case of specular reflective mass is conserved, also in our discrete scheme. The proofs can be found in [18].

6. Numerical Experiments

We have implemented all the techniques discussed in C++. The finite element part is taken from the `deal.II` library [2]. The collision operator is independent of \mathbf{x} and it is thus natural to parallelize via domain decomposition in the spatial domain. The system matrix arising from the advection problem is assembled once and reused in every time-step. We use a block-diagonal, incomplete LU-factorization as preconditioner. Often it is observed that the ILU-preconditioned¹ GMRES solver converges in less than 5 iterations. We use the distributed vectors, sparse matrices, iterative solvers and preconditioners offered by Trilinos v12.2.1 [19].

The numerical experiments in this section are carried out for Maxwellian molecules. The entries of the collision tensor were computed with 81, 131 quadrature points in radial direction and angular direction. For the inner integral (4.7) 131 quadrature points were used. It can thus be assumed that the quadrature error is negligible.

¹Block-diagonal ILU preconditioner with zero fill-in from Trilinos IFPACK.

6.1. Homogeneous case

In order to validate the implementation of the collision operator and to study the approximation properties of the Polar-Laguerre basis, we consider the homogeneous Boltzmann equation

$$\partial_t f = Q(f, f), \quad (6.1)$$

for which a non-stationary, analytical solution is available. This is the so-called BKW solution:

$$f(t, \mathbf{v}; T) = e^{-\frac{\|\mathbf{v}\|^2}{2Ts}} \frac{\|\mathbf{v}\|^2 - s((2 - 4s)T + \|\mathbf{v}\|^2)}{2Ts^3}, \quad t > 0 \quad (6.2)$$

where $s = 1 - \exp(-\frac{\pi T}{4}t - \log 2)$ and T denotes the temperature. It is valid for Maxwellian molecules. For $t \rightarrow \infty$ it converges to

$$\lim_{t \rightarrow \infty} f(t, \mathbf{v}; T) = e^{-\frac{\|\mathbf{v}\|^2}{2T}}. \quad (6.3)$$

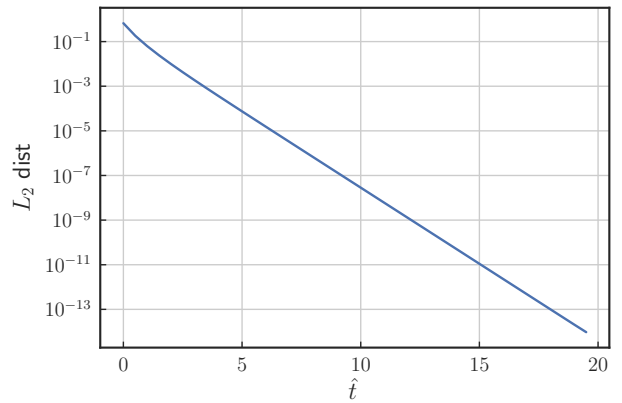
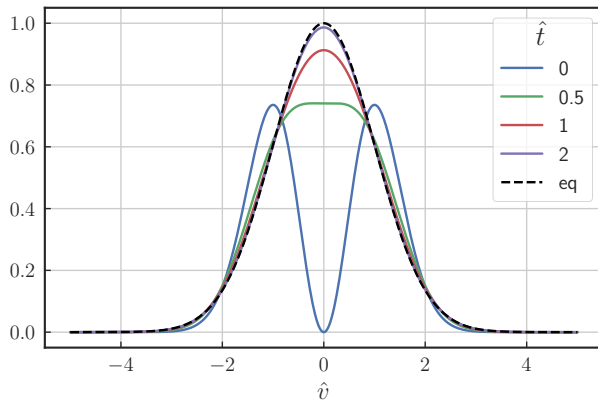
For $T = 1$, it can be represented by a single non-zero coefficient in the Polar-Laguerre basis. The time evolution of the BKW solution is shown in Figure 6.1 using the normalized time $\hat{t} = Tt$.

Theorem 6.1. [13] *Let $f(t, \mathbf{v})$ be a solution to $\partial_t f = Q(f, f)$ with a collision kernel of the form (2.11). Let $\alpha, \gamma > 0$ be given, and define $\eta = \alpha/\gamma^{\lambda+2}$. Then*

$$h(t, \mathbf{v}) = \alpha f(\eta t, \gamma \mathbf{v})$$

is also a solution to (4.1).

In the homogeneous setting, every initial condition can be rescaled to unit temperature using the above theorem. Because of the tensor-product ansatz this is not possible in the inhomogeneous case. In order to demonstrate the approximation properties of the Polar-Laguerre basis, we integrate 4.1 using 4th-order Runge-Kutta timestepping for various BKW initial conditions $f(0, \mathbf{v}; T)$ with temperatures $T \in [\frac{1}{2}, \dots, 4]$ and $\Delta t = 2.5 \times 10^{-3}/T$. The results are given for the Lagrange-multiplier method described in Section 4.2. Relative L_2 -errors are reported in Fig. 6.2, we observe exponential convergence in K . For $K = 48, 56$ and temperatures in $1 \leq T \leq 2$, we obtain errors of the order of the machine precision. For $T = 0.5$, $K = 14$, cf. Fig. 6.2a, we observe numerical blow-up, this is because the L_2 -projection of the BKW solution at $t = 0$ attains negative values.



(A) BKW solution at different times $\hat{t} := Tt$, $\hat{v} := \sqrt{T}^{-1}v$. The dashed line (eq) shows equilibrium solution.

(B) L_2 distance to the equilibrium solution.

FIGURE 6.1. Time evolution of the BKW solution.

n_f	N_f	K	N
10	100	14	105
18	324	25	325
24	576	33	561
28	784	39	780
34	1,156	48	1,176
40	1,600	56	1,596

TABLE 6.1. Comparison with the Fourier spectral method: Degrees of freedom for Fourier $N_f = n_f^2$ (left) and Polar-Laguerre basis $N = K(K + 1)/2$ (right).

Comparison with the Fourier spectral method. The classical Fourier spectral method [26, 11] is known to converge to a constant distribution in velocity for long times [7, Rem. 5.13]. This behaviour can be avoided by the steady state preserving scheme [12], it makes use of the decomposition

$$f = M + g, \tag{6.4}$$

where M is a local Maxwellian equilibrium and g such that $\int_{\mathbb{R}^2} g \phi \, d\mathbf{v} = 0$, $\phi(\mathbf{v}) := 0, \mathbf{v}, \|\mathbf{v}\|^2$. Inserting this into the collision operator gives

$$Q(f, f) = \mathcal{L}(M, g) + Q(g, g) + Q(M, M), \tag{6.5}$$

where $\mathcal{L}(M, g) = Q(g, M) + Q(M, g)$. The steady state preserving (SSP) scheme then reads

$$\begin{cases} \frac{\partial g}{\partial t} = \mathcal{L}(M, g) + Q(g, g), \\ f = M + g. \end{cases} \tag{6.6}$$

Note that this is identical to the classical Fourier method, except that the constant in time term $Q(M, M)$ has been removed, which is zero in the continuous case and spectrally small in the Fourier representation. As the original scheme it conserves mass and momentum. In order to conserve energy the Lagrange multiplier, cf. Section 4.2, method can be used for both formulations. For the Fourier spectral method we truncate the velocity distribution to a box of size $L = 2\sqrt{T^{-1}} [-1, 1]^2$. The domain of the collision operator is restricted to $[-R, R]^2$, where $R = \lambda L$, $\lambda = \frac{2}{3+\sqrt{2}}$.

Fig. 6.3 shows L_2 -errors computed for the BKW solution using the Polar-Laguerre and the Fourier spectral method using both the classical and the SSP variant. The number of Polar-Laguerre basis functions is chosen such that the number of total degrees of freedom for both methods are roughly equal, cf. Table 6.1. For $t \rightarrow \infty$ the Polar-Laguerre method converges to a Maxwellian determined by $\rho(t=0)$, $\mathbf{u}(t=0)$, $E(t=0)$, whereas the classical Fourier method converges to a constant distribution in velocity [7, Rem. 5.13] due to aliasing errors. Indeed, increasing errors for long times are observed for $n_f < 40$ Fourier modes using the classical Fourier method. Applying the Lagrange multiplier method to conserve energy does not help to reduce this effect. The SSP scheme gives the same accuracy, but errors do not increase over time.

6.2. Supersonic flow in a wind tunnel

We show numerical results for a supersonic flow in the hydrodynamic regime, $\epsilon = 2.5 \times 10^{-3}$, over a forward facing step in 2D. The experiment was first introduced in [8]. The computational domain describes a wind tunnel with a step at position $x = 0.6$ with height 0.2. The gas is initially in equilibrium with temperature $T_0=1, \mathbf{v}=[3, 0]$, $\rho = 1.4$. At $x=0$ inflow boundary conditions with

$T=1$, $\mathbf{v}=[3, 0]$, $\rho=1.4$ are imposed and outflow (zero inflow) boundary conditions at $x=3$, the other walls are specularly reflective. In Fig. 6.5 the pressure is shown at different times $t \in [0, 1]$. We have used a time-step of length $\Delta t=2.5 \times 10^{-5}$. Fig. 6.6 displays the comparison of the macroscopic density with the reference solution obtained from a high-order finite volume solver for the Euler equations (FVM MUSCL scheme) [21]. The positions of the shock waves are accurately reproduced by the Boltzmann solver. The contour lines in the rarefaction wave differ, this can be explained by the huge difference in the degrees of freedom, the Euler solver uses 3×10^6 cells in the spatial domain versus 3.5×10^3 DoFs for the Boltzmann solver. Additionally, the choice of continuous finite elements in the spatial domain makes it impossible to satisfy the boundary conditions at the corners. On coarse meshes, we have observed that the distribution function can become negative at the re-entrant corner. Especially for small Knudsen numbers, for example $\epsilon=2.5 \times 10^{-3}$, this can cause the solution to diverge when the collision operator is applied. A possible remedy is to project onto positive distribution values in \mathbf{v} , see discussion below. The projection step was not required for the results reported here. The relative L_2 -errors for two different spatial resolutions and $K = 20, \dots, 40$ are shown Figure 6.4.

Ensuring positivity. We have observed that in the vicinity of singularities, for example near re-entrant corners, the distribution function might become negative locally. In combination with a low Knudsen number this can cause numerical blow-up of the solution by the collision operator. A possible remedy is to evaluate the distribution function after each time-step at the quadrature nodes, set negative values to zero and project back onto the Polar-Laguerre basis. A naive implementation requires the evaluation of $f(\mathbf{v})$ at $\mathcal{O}(K^2)$ quadrature nodes, whereas the evaluation requires $\mathcal{O}(K^2)$ operations per node and thus has a total cost of $\mathcal{O}(K^4)$. The algorithms developed in [14] provide an elegant solution by transforming first to the Hermite and then to the nodal basis. As already noted in Section 4.4, the transformation between the Polar-Laguerre and the Hermite basis can be done with effort $\mathcal{O}(K^3)$. The transformation between the Hermite and nodal basis again costs $\mathcal{O}(K^3)$, this time because it can be performed separately along each coordinate axis and therefore the transformation matrices are of size $K \times K$ only. The entries of the Hermite to nodal transformation matrix $\mathbf{T}_{\mathbf{H} \rightarrow \mathbf{N}} \in \mathbb{R}^{K,K}$ are given by:

$$(\mathbf{T}_{\mathbf{H} \rightarrow \mathbf{N}})_{i,j} = \int_{\mathbb{R}} h_j(x) e^{-\frac{x^2}{2}} \ell_i(x) e^{-\frac{x^2}{2}} dx = \sum_{k=0}^K h_j(x_k) \ell_i(x_k) w_k = \sum_{k=0}^K h_j(x_k) \frac{\delta_{i,k}}{\sqrt{w_k}} w_k = h_j(x_i) \sqrt{w_i}, \quad (6.7)$$

where $x_i, w_i, i = 0, \dots, K$ are the Gauss-Hermite quadrature nodes and weights. We have that $(\mathbf{T}_{\mathbf{N} \rightarrow \mathbf{H}})^{-1} := \mathbf{T}_{\mathbf{H} \rightarrow \mathbf{N}}^T$, since $\mathbf{T}_{\mathbf{H} \rightarrow \mathbf{N}}$ is an orthonormal matrix:

$$\begin{aligned}
 (\mathbf{T}_{\mathbf{H} \rightarrow \mathbf{N}})^T \mathbf{T}_{\mathbf{H} \rightarrow \mathbf{N}} &= \sum_{k=0}^K (h_i(x_k) \sqrt{w_k}) (h_j(x_k) \sqrt{w_k}) = \sum_{k=0}^K h_i(x_k) h_j(x_k) w_k \\
 &= \int_{\mathbb{R}^2} h_i(x) h_j(x) e^{-x^2} dx = \delta_{i,j} \quad (6.8)
 \end{aligned}$$

6.3. Nozzle flow

We consider the flow of a rarefied gas with $\epsilon = 0.1$ in a nozzle, see Fig. 6.7. Inflow boundary conditions are placed at the left boundary with $T = 1$, $\mathbf{v}_0 = [2.5, 0]$, $\rho_0 = 1.4$, and outflow b.c. at $x = 4$, the

Algorithm 2 Project to positive velocity distribution values

```

1: procedure APPLY THE COLLISION OP. IN RE-CENTERED BASIS( $\mathbf{c}^P$ )
2:    $\mathbf{c}^H \leftarrow \mathbf{T}_{P \rightarrow H} \mathbf{c}^P$  ▷ Transform to Hermite basis
3:    $\mathbf{c}^N \leftarrow \mathbf{T}_{H \rightarrow N} \mathbf{c}^H$  ▷ Transform to Nodal basis
4:   for all  $(\mathbf{c}^N)_i < 0$  do
5:      $(\mathbf{c}^N)_i \leftarrow 0$  ▷ Set negative coefficients to zero
6:   end for
7:    $\mathbf{c}^H \leftarrow \mathbf{T}_{N \rightarrow H} \mathbf{c}^N$  ▷ Transform to Hermite basis
8:    $\mathbf{c}^P \leftarrow \mathbf{T}_{H \rightarrow P} \mathbf{c}^H$  ▷ Transform to Polar-Laguerre basis
9: end procedure

```

other walls are specularly reflecting. The initial distribution was

$$f(t=0, \mathbf{x}, \mathbf{v}) = \frac{\rho_0}{2\pi} \exp\left(-\frac{1}{2} \|\mathbf{v} - \mathbf{v}_0\|^2\right). \quad (6.9)$$

Convergence plots for the L_2 -errors are reported in Fig. 6.8, the reference solution was computed on a mesh with 18 500 vertices and for polynomial degree $K=40$. For the lowest resolution in space, i.e. $L=1200$ and for $K > 26$, we find that the error is dominated by the mesh size, whereas for $L=4700$ the errors mainly depend on K . Compared to the supersonic flow experiment in Section 6.2, we obtain smaller errors and faster convergence with respect to K , which is attributed to the absence of shocks.

6.4. Shock tube

A gas is filled into a tube of unit length. Initially the gas is at equilibrium in the left and right half with densities ρ_l, ρ_r and temperatures T_l, T_r :

$$\begin{aligned}
 f_l(t=0, \mathbf{x}, \mathbf{v}) &= \frac{\rho_l}{2\pi T_l} \exp\left(-\frac{\|\mathbf{v}\|^2}{2T_l}\right), & x < 0.5 \\
 f_r(t=0, \mathbf{x}, \mathbf{v}) &= \frac{\rho_r}{2\pi T_r} \exp\left(-\frac{\|\mathbf{v}\|^2}{2T_r}\right), & x \geq 0.5,
 \end{aligned} \quad (6.10)$$

where $\rho_l=1, \rho_r=1$ and $T_l=1.25, T_r=1$. Specular reflective boundary conditions are imposed on the top and bottom wall, at $x=0, x=1$ we use inflow boundary conditions with densities ρ_l, ρ_r and temperatures T_l, T_r . The calculations were carried out on a structured grid with element size $h_x=1.48 \times 10^{-3}$ in x -direction for different $\epsilon=0.01, 0.1, 1$, and with polynomial degrees $K=16, 20, 26, 30, 36, 40$. The calculation with $K=40$ is used as reference to compute L_2 -errors in the VDF $f(\mathbf{v}, \mathbf{x})$ and for the macroscopic quantities $\rho, |\mathbf{u}|$ and E . L_2 -errors are shown in Fig. 6.9, the errors for $\epsilon=0.01$ are an order of magnitude smaller compared to the calculations with $\epsilon=0.1$. This is because for $\epsilon=0.01$, the smoothing by the collision operator is stronger and therefore better approximation in the velocity domain is obtained. In Fig. 6.10, the density and momentum \mathbf{u}_x are compared for $K=30, 40$ at different times along the line $x(s)=s, s \in [0, 1]$. Note that the sluggish convergence observed in Fig. 6.9 is due to the Gibbs phenomenon.

6.5. Propagation of discontinuities

We consider the Boltzmann equation in one space dimension, $x \in [0, 1]$:

$$\begin{cases} \frac{\partial f}{\partial t} + v_x \frac{\partial f}{\partial x} = \frac{1}{\epsilon} Q(f, f) \\ f(t = 0, x, \mathbf{v}) = \frac{1}{2\pi T_0} \exp\left(-\frac{|\mathbf{v}|^2}{2T_0}\right) \end{cases} \quad (6.11)$$

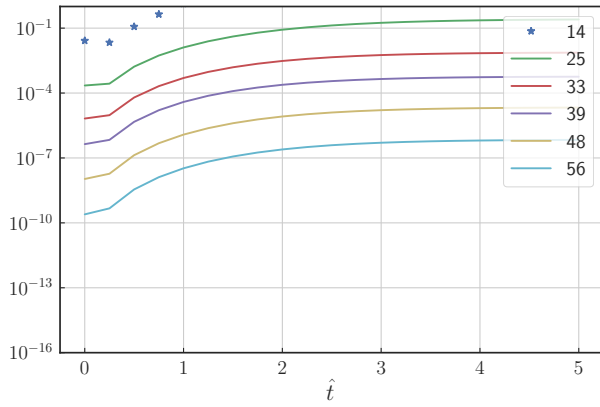
At time $t = 0$, a sudden change in the wall temperature $T_w = 2T_0$ is imposed in $x = 0$, where $T_0 = 1$, $\epsilon = 0.1$. Specular reflective boundary conditions are used at the right wall in $x = 1$. The numerical experiments were performed for various polynomial degrees and 1024 grid points in x using a timestep $\Delta t = 10^{-3}$. The distribution function $f(\mathbf{v})$ close to the left wall at $x = 0.04$ is shown Fig. 6.11, results for the macroscopic velocity \mathbf{v}_x and density ρ are depicted in Fig. 6.12. We observe good qualitative agreement in the distribution function and macroscopic quantities for polynomial degrees $K = 20, \dots, 60$. The same numerical experiment for the Fourier spectral method can be found in [10], where $n = 32, 128$ Fourier modes in each direction were used. For the Fourier spectral method, there is no difference visible (between $n = 32$ and 128) in the plots of the macroscopic quantities, which is not the case for our method.

6.6. Flow generated by a temperature gradient

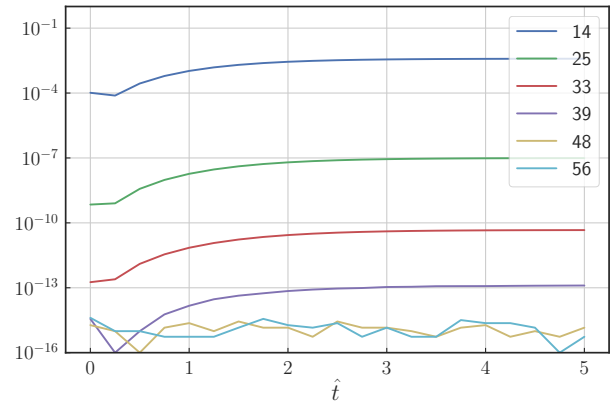
We consider an infinite slab with thickness $d = 1$ and diffusive reflective boundary conditions with temperatures $T_l=1, T_u=1.44$ at the lower and upper wall. We choose the initial condition as follows in order to avoid the Gibbs phenomenon from the previous example:

$$\begin{aligned} f(t = 0, y, \mathbf{v}) &= \frac{1}{2\pi T(y)} e^{-\frac{\|\mathbf{v}\|^2}{2T(y)}}, \\ T(y) &= 1 + 1.44y. \end{aligned} \quad (6.12)$$

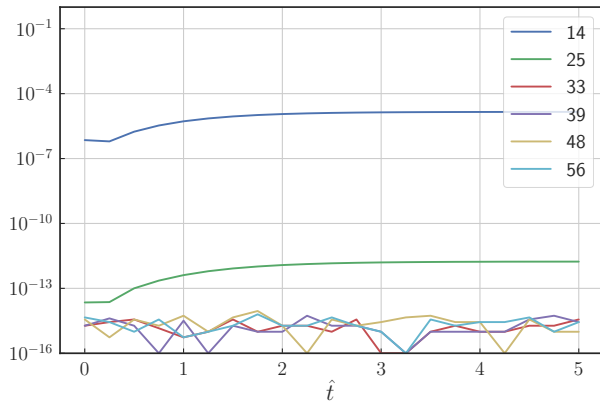
The simulations were carried out for Knudsen numbers $\epsilon = 0.025, 0.1, 1$, until a stationary state was reached with time-step $\Delta t = 10^{-3}$. We observe good agreement in the temperature profiles for $K = 20, \dots, 40$ and with results obtained in [10].



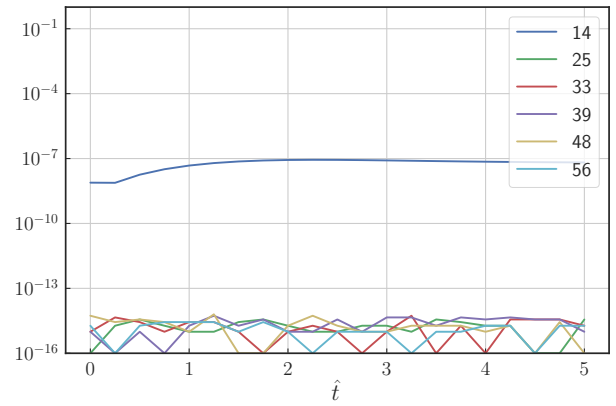
(A) $T = 0.5$



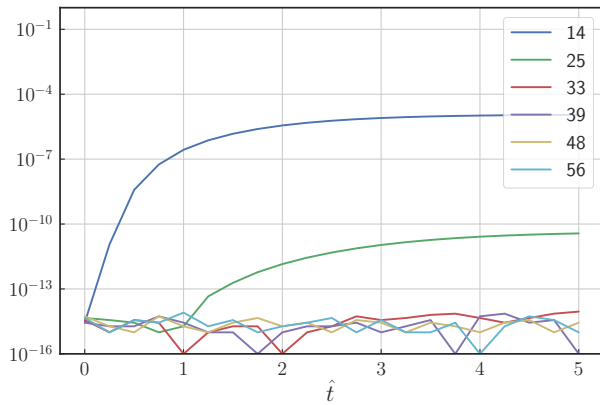
(B) $T = 1$



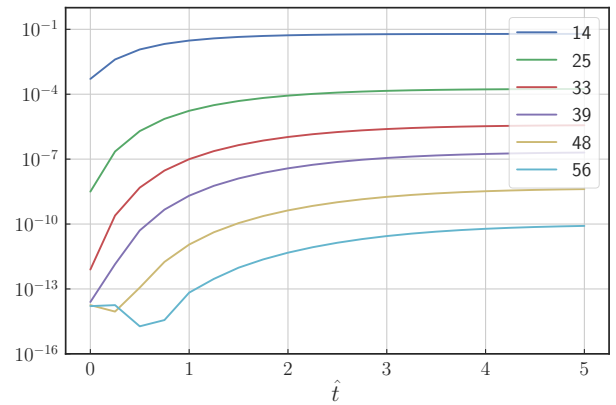
(C) $T = 1.3$



(D) $T = 1.5$



(E) $T = 2$



(F) $T = 4$

FIGURE 6.2. BKW solution rescaled to different temperatures T : Squared L_2 -errors for different polynomial degrees K . (Temperature) normalized time $\hat{t} := T t$. The curves represented by a star suffer from numerical blow up due to locally negative distribution values in the initial projection.

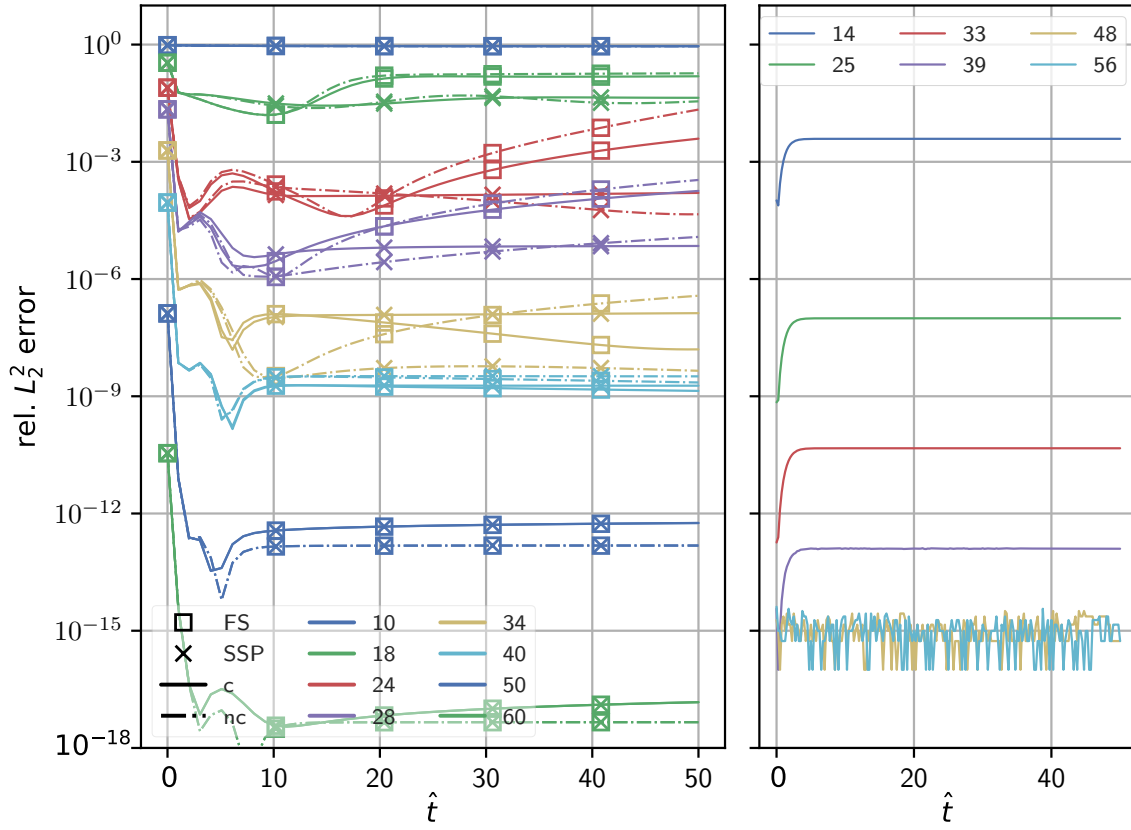
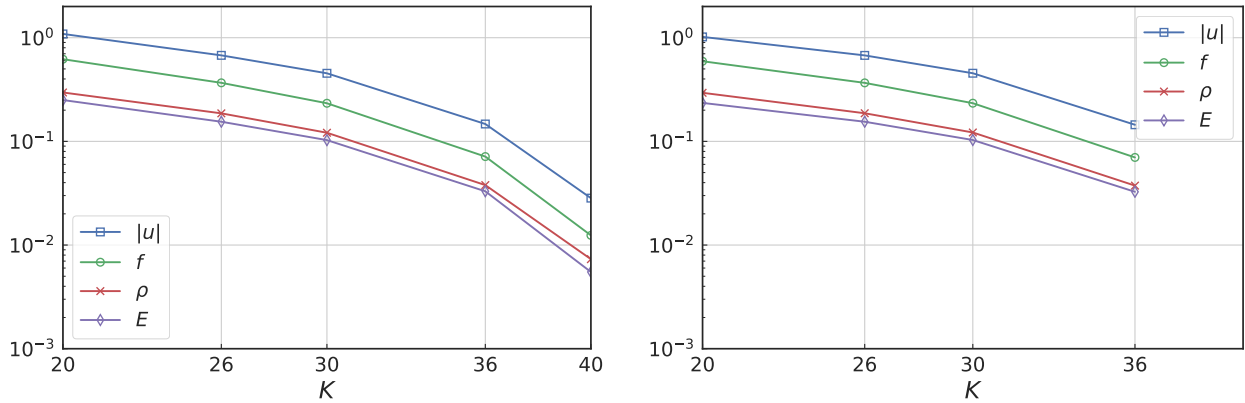


FIGURE 6.3. Comparison of the Fourier spectral (left) and Polar-Laguerre (right) method: squared relative L_2 -errors for the BKW solution at temperature $T = 1$. FS: plain Fourier spectral method, SSP: steady state preserving Fourier spectral method. c: conservation of energy enforced by Lagrange multipliers, nc: without Lagrange multipliers for conservation of energy.



(A) Number of spatial DoFs: $L=8945$

(B) Number of spatial DoFs: $L=35297$

FIGURE 6.4. Supersonic flow in a wind tunnel: relative L_2 -errors vs. polynomial degree K for two spatial grids with different numbers of vertices. The solution on the finest grid with highest polynomial degree $K=40$ was used as reference. Errors are shown for the velocity distribution function f and the macroscopic observables: mass ρ , momentum \mathbf{u} and energy E . The errors are dominated by the polynomial degree K .

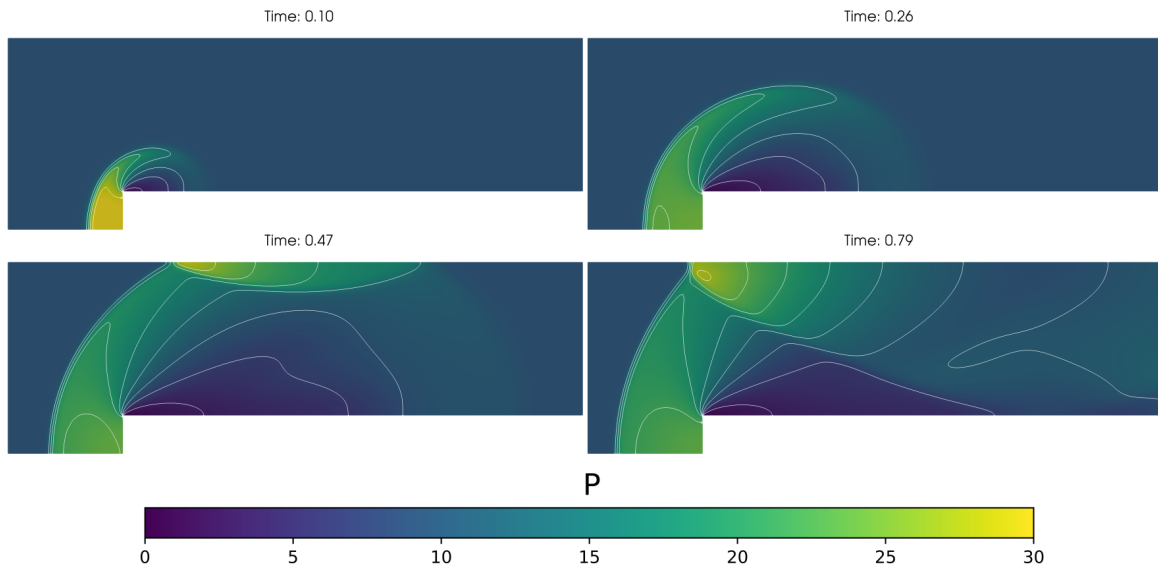


FIGURE 6.5. Supersonic flow in a wind tunnel: polynomial degree $K = 40$, 35k vertices, Maxwellian molecules, 28.9M total DoFs. Coloring: pressure, contour lines: density. Computations were carried out on the Euler cluster of ETH Zurich (Xeon E5-2697 v2) using 360 cores.

TENSOR-PRODUCT DISCRETIZATION FOR THE BOLTZMANN EQUATION

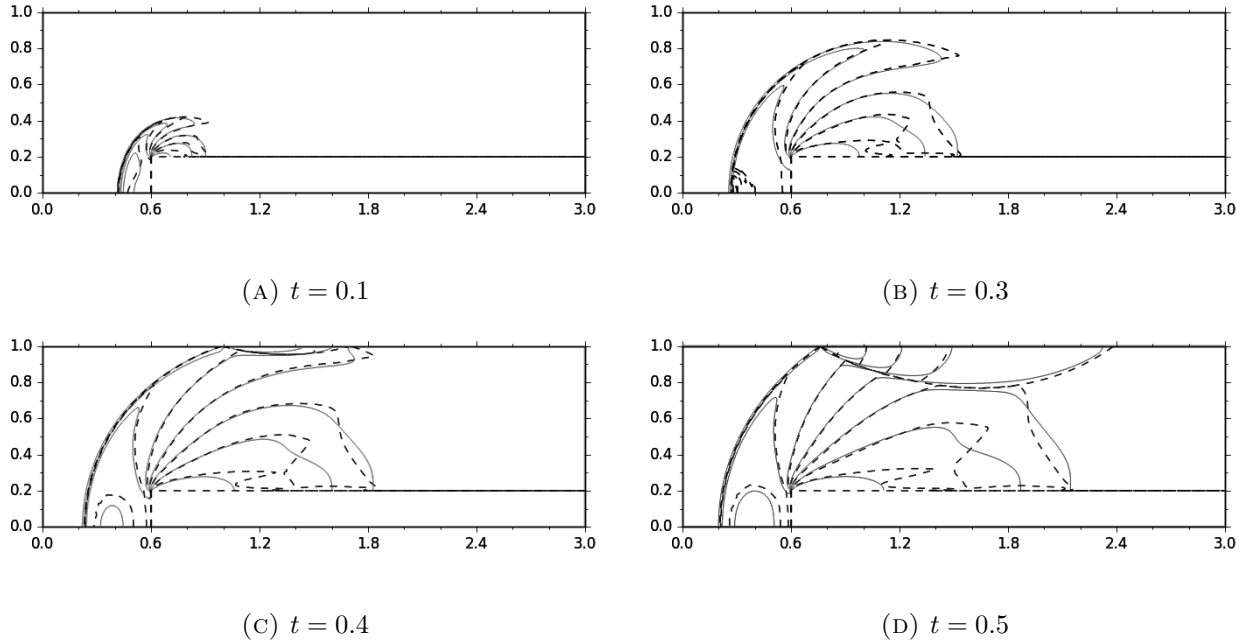


FIGURE 6.6. Supersonic flow in a wind tunnel: Contour lines of the macroscopic density ρ at different times. **Dashed** lines: reference solution for the Euler eqs. (FVM MUSCL scheme) (1024×3072 cells). **Solid** lines: Boltzmann eq. ($35k \times 820$ DoFs in $V_D^L \times V_V^N$).

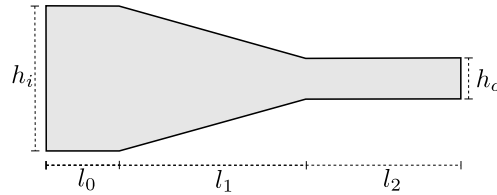


FIGURE 6.7. Nozzle domain: Inflow BC on the left boundary, outflow on the right. $h_i = 1.4$, $h_o = 0.4$, $l_0 = 0.7$, $l_1 = 1.8$, $l_2 = 1.5$

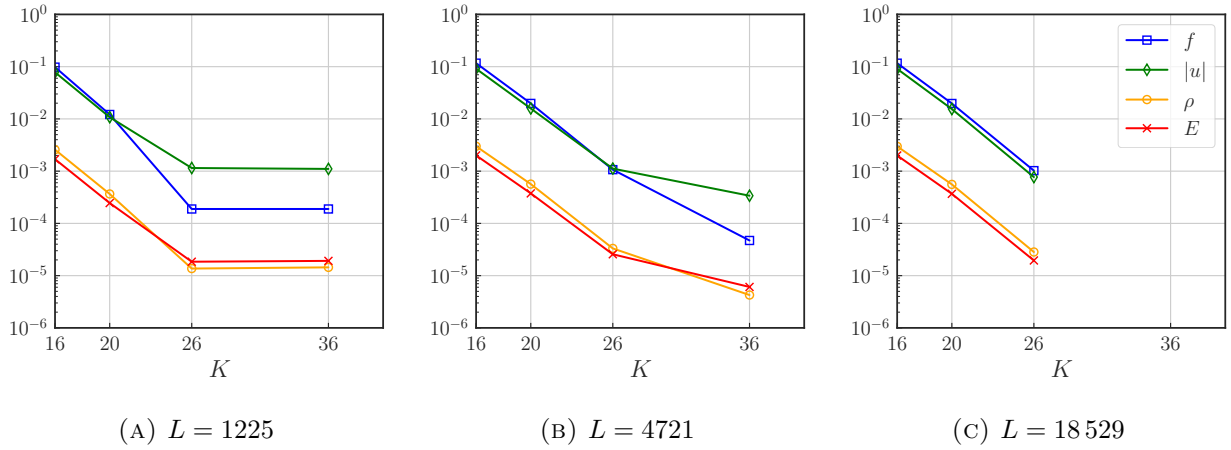


FIGURE 6.8. Nozzle flow: relative L_2 -errors at time $t = 3.75$. Reference solution with $K = 40, L = 18529, \Delta t = 2.5 \times 10^{-4}$.

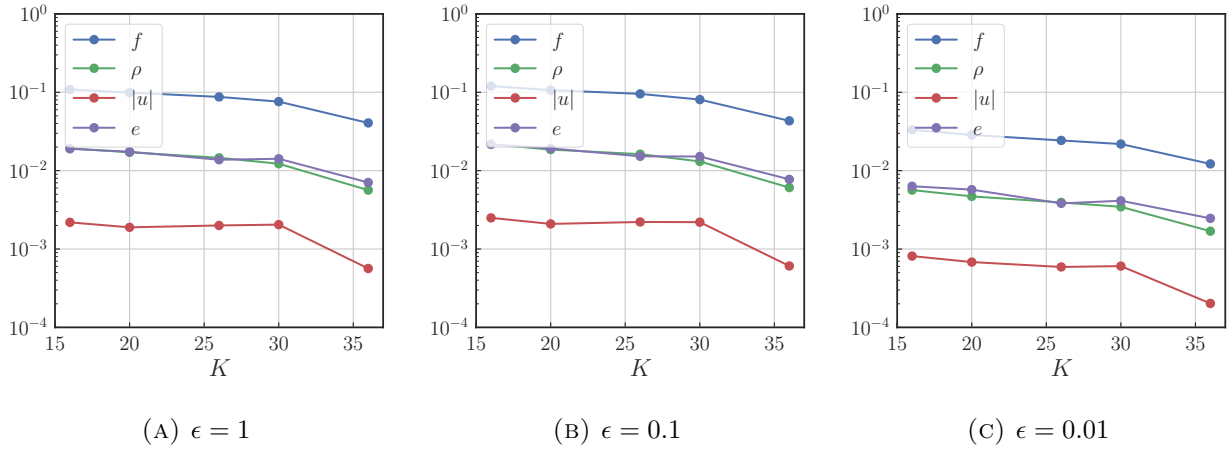


FIGURE 6.9. Relative L_2 -errors for the shock tube with varying polynomial degree K . Reference computation with $K=40$ at time $t=0.1$.

Tensor-Product Discretization for the Boltzmann Equation

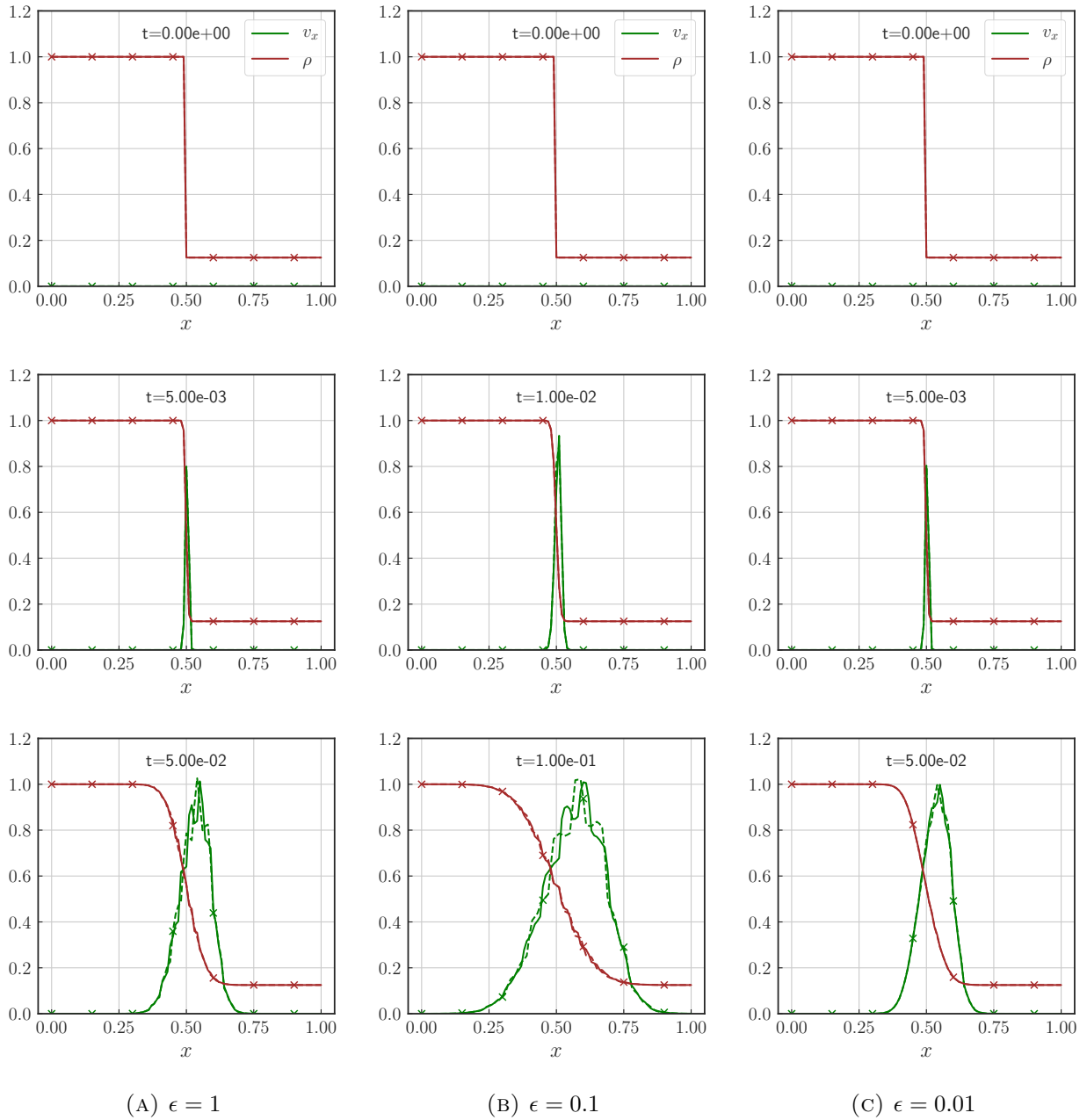
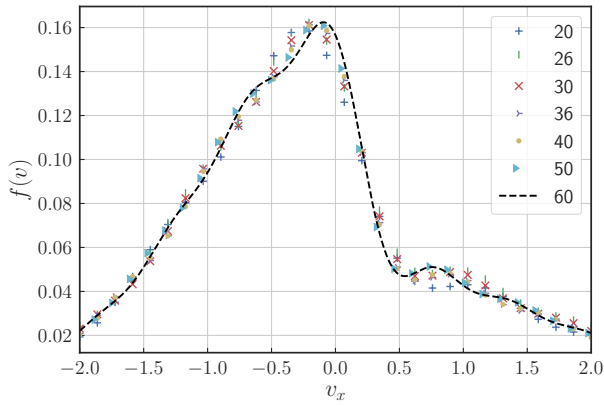
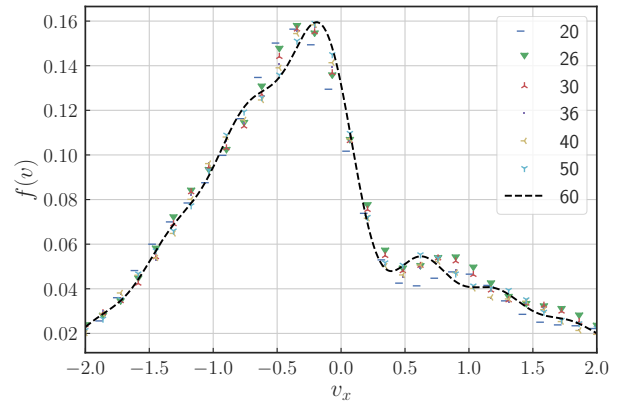


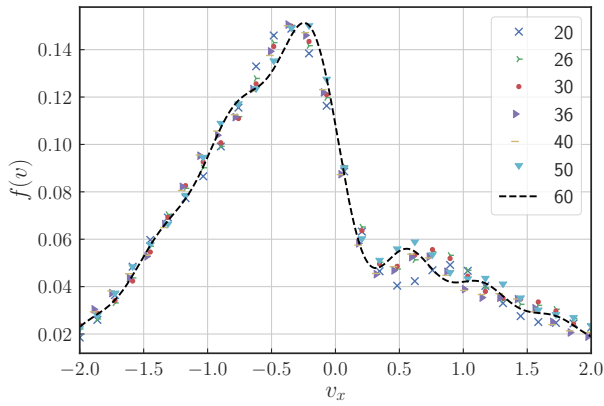
FIGURE 6.10. Shock tube: Macroscopic density and momentum in x -direction plotted along the line $x = [0, 1]$. **Solid line:** Polynomial degree $K = 40$, **Dashed line:** $K = 30$



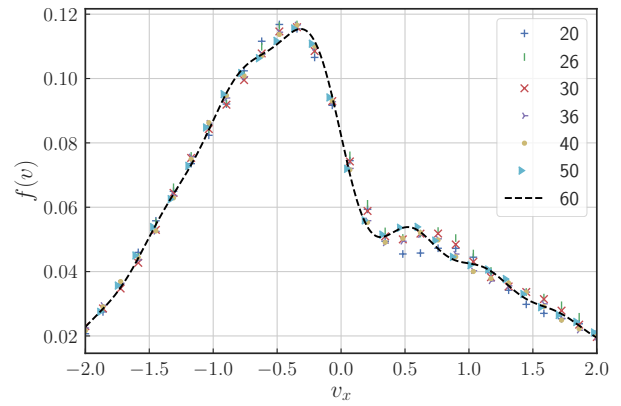
(A) $f(\mathbf{v}, t = 0.02)$



(B) $f(\mathbf{v}, t = 0.04)$



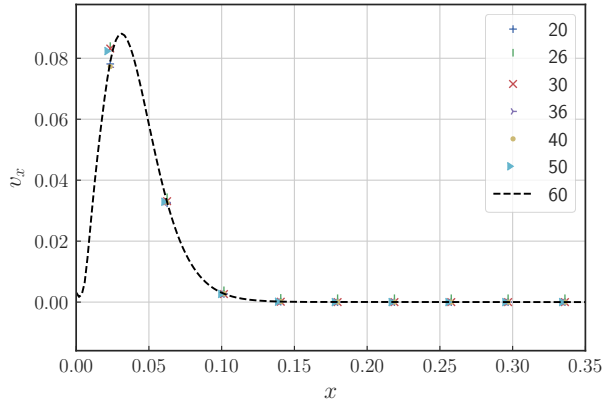
(C) $f(\mathbf{v}, t = 0.1)$



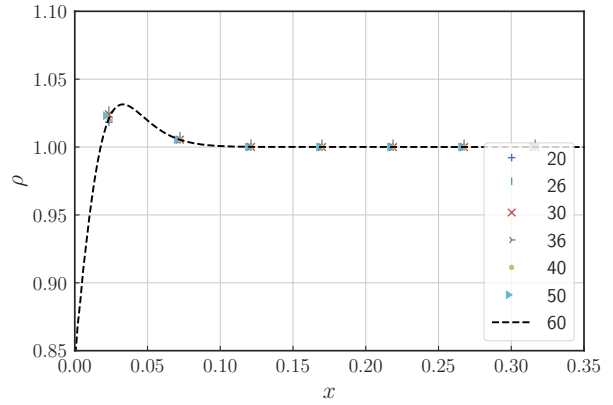
(D) $f(\mathbf{v}, t = 0.5)$

FIGURE 6.11. Propagation of discontinuities: Distribution function $f(\mathbf{v}, t)$ at $x = 0.004$ for different polynomial degrees K .

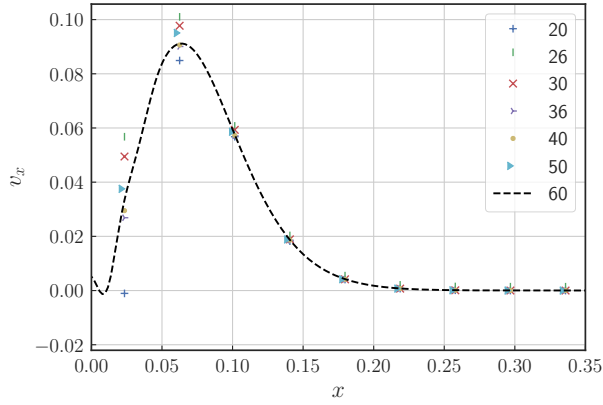
Tensor-product discretization for the Boltzmann equation



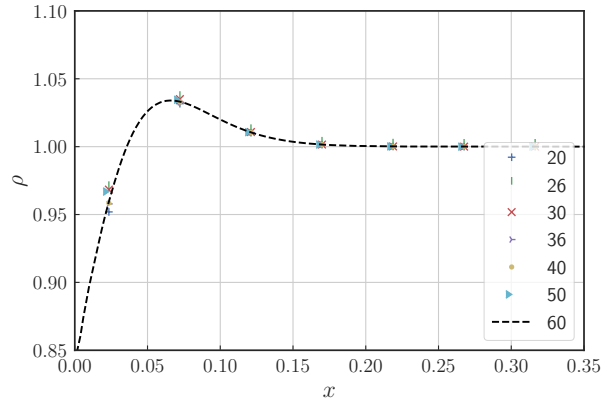
(A) Velocity v_x , $t = 0.02$



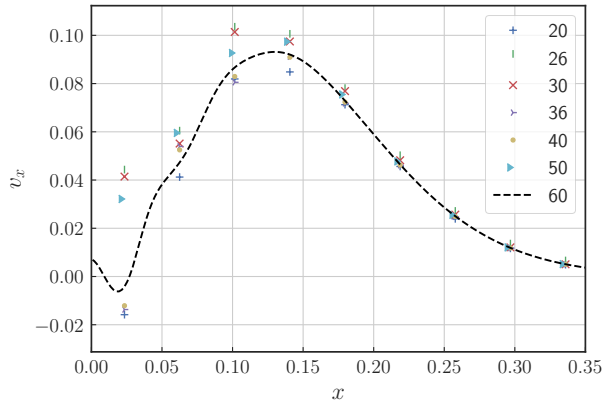
(B) Density ρ , $t = 0.02$



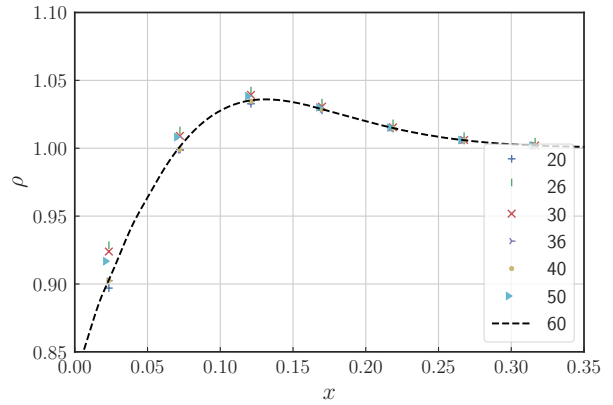
(C) Velocity v_x , $t = 0.04$



(D) Density ρ , $t = 0.04$



(E) Velocity v_x , $t = 0.08$



(F) Density ρ , $t = 0.08$

FIGURE 6.12. Propagation of discontinuities: Macroscopic velocity and density for different polynomial degrees K .

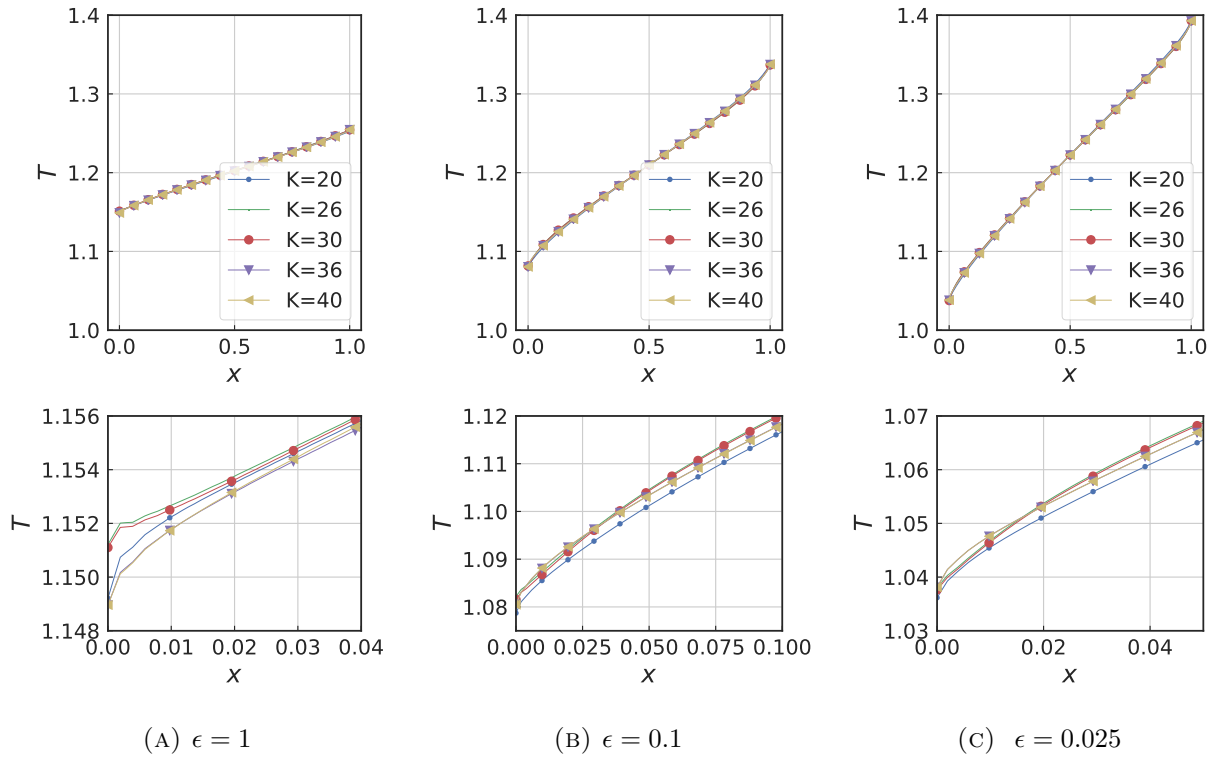


FIGURE 6.13. Flow generated by a temperature gradient: Temperature profiles for the stationary states at time $t = 6, 25, 75$ for $\epsilon = 1, \frac{1}{10}, \frac{1}{40}$. The lower row shows $T(x)$ close to the left boundary.

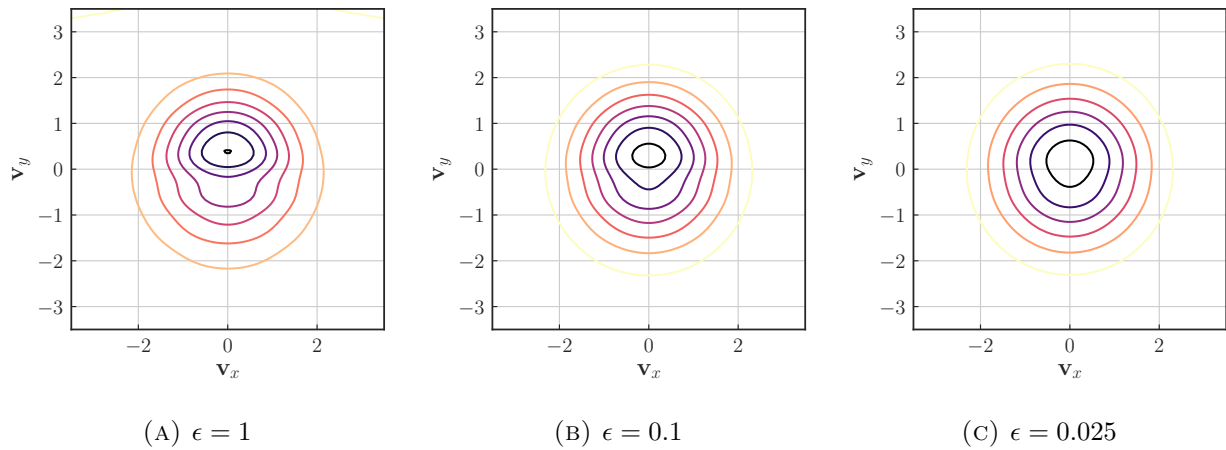


FIGURE 6.14. Flow generated by a temperature gradient: Mass distribution function at the upper wall: $f(t=t_{\text{end}}, y=1, \mathbf{v})$.

7. Conclusion

We have presented a combined spectral polynomial and finite element method for the spatially inhomogeneous Boltzmann equation. It can be extended to conserve the lowest moments and include all relevant boundary conditions. We have elaborated it for elastic collisions in the variable hard spheres model. The simulations were carried out for Maxwellian molecules, but in general, any sufficiently regular separable collision kernel of the form $C(\cos \theta) \|\mathbf{v} - \mathbf{v}_*\|^\lambda$, $\lambda \geq 0$ can be tackled by our scheme. Conservation of mass, momentum and energy can be achieved by the Lagrange multiplier method. For numerical testing we have implemented an extensive simulation framework in C++ which can deal with different types of boundary conditions on realistic geometries in $2D$. The code has been parallelized using MPI, and provided that the spatial mesh is sufficiently fine, scales well up to a few hundred processors. Details of this implementation will be published separately. We have reported numerical results for low and high-speed flows from the hydrodynamic to the rarefied regime. The polar spectral basis offers fast convergence for smooth solutions. For initial distributions with discontinuities we observe a degradation in convergence with respect to the velocity degrees of freedom. The same holds true for discontinuities in the velocity distribution function imposed by hot or cold walls.

References

- [1] M. Abramowitz and I. Stegun. *Handbook of Mathematical Functions*. Dover, June 1972.
- [2] W. Bangerth, T. Heister, L. Heltai, G. Kanschat, M. Kronbichler, M. Maier, and B. Turcksin. The deal.ii library, version 8.3. *Archive of Numerical Software*, 4(100):1–11, 2016.
- [3] G. A Bird. *Molecular Gas Dynamics And The Direct Simulation Of Gas Flows*. Clarendon Press; Oxford University Press, 1994.
- [4] A. Bobylev and S. Rjasanow. Difference scheme for the Boltzmann equation based on the Fast Fourier Transform. *European Journal of Mechanics, B/Fluids*, 16(2):293–306, 1997.
- [5] A. V. Bobylev and S. Rjasanow. Fast deterministic method of solving the Boltzmann equation for hard spheres. *Eur. J. Mech. B. Fluids*, 18(5):869–887, September 1999.
- [6] C. Cercignani. Chapter 1 - The Boltzmann Equation and Fluid Dynamics. In S. Friedlander D. Serre, editor, *Handbook of Mathematical Fluid Dynamics*, volume 1, pages 1–69. North-Holland, 2002.
- [7] G. Dimarco and L. Pareschi. Numerical methods for kinetic equations. *Acta Numerica*, 23:369–520, 2014.
- [8] A. F. Emery. An evaluation of several differencing methods for inviscid fluid flow problems. *J. Comput. Phys.*, 2(3):306–331, February 1968.
- [9] A. Ya Ender and I. A. Ender. Polynomial expansions for the isotropic Boltzmann equation and invariance of the collision integral with respect to the choice of basis functions. *Physics of Fluids (1994-present)*, 11(9):2720–2730, September 1999.
- [10] F. Filbet. On deterministic approximation of the Boltzmann equation in a bounded domain. *Multiscale Modeling & Simulation*, 10(3):792–817, January 2012.
- [11] F. Filbet, C. Mouhot, and L. Pareschi. Solving the Boltzmann equation in $N \log N$. *SIAM J. Sci. Comput.*, 28(3):1029–1053, January 2006.
- [12] F. Filbet, L. Pareschi, and T. Rey. On steady-state preserving spectral methods for homogeneous Boltzmann equations. *C.R. Math.*, 353(4):309–314, April 2015.
- [13] E. Fonn, P. Grohs, and R. Hiptmair. Polar spectral scheme for the spatially homogeneous Boltzmann equation. Technical Report 2014-13, Seminar for Applied Mathematics, ETH Zürich, Switzerland, 2014.
- [14] G. Kitzler and J. Schöberl. Efficient spectral methods for the spatially homogeneous Boltzmann equation. Technical Report 13/2013, Institute for Analysis and Scientific Computing, TU Wien, Austria, 2013.

- [15] I. M. Gamba and S. H. Tharkabhushanam. Spectral-Lagrangian methods for collisional models of non-equilibrium statistical states. *J. Comput. Phys.*, 228(6):2012–2036, April 2009.
- [16] G. H. Golub and J. H. Welsch. Calculation of Gauss quadrature rules. *Math. Comput.*, 23(106):221–s10, 1969.
- [17] H. Grad. Principles of the kinetic theory of gases. In S. Flügge, editor, *Thermodynamics of Gases*, number 3 / 12 in Encyclopedia of Physics, pages 205–294. Springer Berlin Heidelberg, 1958.
- [18] P. Grohs, R. Hiptmair, and S. Pintarelli. Tensor-product discretization for the spatially inhomogeneous and transient Boltzmann equation in 2d. Technical Report 2015-38, Seminar for Applied Mathematics, ETH Zürich, Switzerland, 2015.
- [19] M.A. Heroux, R. A. Bartlett, V. E. Howle, R. J. Hoekstra, J. J. Hu, T. G. Kolda, R. B. Lehoucq, K. R. Long, R. P. Pawlowski, E. T. Phipps, A. G. Salinger, H. K. Thornquist, R. S. Tuminaro, J. M. Willenbring, A. Williams, and K. S. Stanley. An overview of the Trilinos project. *ACM Trans. Math. Softw.*, 31(3):397–423, 2005.
- [20] T. Jahnke and C. Lubich. Error Bounds for Exponential Operator Splittings. *BIT Numerical Mathematics*, 40(4):735–744, December 2000.
- [21] R. Käppeli, S. C. Whitehouse, S. Scheidegger, U.-L. Pen, and M. Liebendörfer. FISH: A Three-dimensional Parallel Magnetohydrodynamics Code for Astrophysical Applications. *The Astrophysical Journal Supplement Series*, 195(2), 2011.
- [22] G. Kitzler and J. Schöberl. A high order space–momentum discontinuous Galerkin method for the Boltzmann equation. *Computers & Mathematics with Applications*, 70(7):1539–1554, October 2015.
- [23] K. Nanbu. Direct simulation scheme derived from the Boltzmann equation. I. Monocomponent Gases. *J. Phys. Soc. Jpn.*, 49(5):2042–2049, November 1980.
- [24] P. B. Bochev and M. D. Gunzburger. *Least-squares finite element methods*, volume 166 of *Applied mathematical sciences*. Springer, 2009.
- [25] L. Pareschi and B. Perthame. A Fourier spectral method for homogeneous Boltzmann equations. *Transp. Theory Stat. Phys.*, 25(3-5):369–382, April 1996.
- [26] L. Pareschi and G. Russo. Numerical Solution of the Boltzmann Equation I: Spectrally Accurate Approximation of the Collision Operator. *SIAM J. Numer. Anal.*, 37(4):1217–1245, January 2000.
- [27] B. Shizgal. A Gaussian quadrature procedure for use in the solution of the Boltzmann equation and related problems. *J. Comput. Phys.*, 41(2):309–328, June 1981.
- [28] C. Villani. A review of mathematical topics in collisional kinetic theory. In S. Friedlander and D. Serre, editors, *Handbook of Mathematical Fluid Dynamics, Vol. 1*, pages 71–305. Elsevier, 2002.
- [29] U. Wiesmann. The spherical Laguerre method for the spatially homogeneous Boltzmann equation. masterthesis, ETH Zurich, 2015.
- [30] L. Wu, C. White, T. J. Scanlon, J. M. Reese, and Y. Zhang. Deterministic numerical solutions of the Boltzmann equation using the fast spectral method. *J. Comput. Phys.*, 250:27–52, October 2013.